

Report on photocatalytic coating

D3.6

02/2019



This project has received funding from the European Union's Horizon 2020 research and innovation programme under grant agreement No 689954.

Project Acronym and Name	iSCAPE - Improving the Smart Control of Air Pollution in Europe	
Grant Agreement Number	689954	
Document Type	Report	
Document version & WP No.	V0.1	WP3
Document Title	Report on photocatalytic coating	
Main authors	Silvana Di Sabatino (Lead UNIBO), Beatrice Pulvirenti (UNIBO), Erika Brattich (UNIBO), Francesco Barbano (UNIBO), Sara Baldazzi (UNIBO), Francesca Di Nicola (UNIBO), Marco Deserti (ARPA-ER), Luca Torreggiani (ARPA-ER), Carla Barbieri (ARPA-ER), Arianna Trentini (ARPA-ER), Vanes Poluzzi (ARPA-ER)	
Partner in charge	UNIBO	
Contributing partners	UNIBO, ARPA-ER	
Release date	28/02/2019	

The publication reflects the author's views. The European Commission is not liable for any use that may be made of the information contained therein.

Document Control Page			
Short Description	<p><i>This report is the output of the work carried out in Task 3.5 of the iSCAPE project whose aim is to examine the effectiveness of the alteration in dispersion conditions influencing the background concentrations in the local area of interest and to calculate the influence of the alteration of dispersion conditions from abatement strategies or alteration of urban canopy around hotspot areas. In particular, Task 3.5 is focused on physical PCSs (Passive Control Systems) such as LBW (Low Boundary Walls) and photocatalytic coatings. This report examines in detail the effectiveness of one of the two PCSs, photocatalytic coating, in a neighborhood of Bologna where a monitoring campaign was carried out during summer 2018. Data gathered during the monitoring campaign, described and thoroughly analysed in D3.8 output of the same Task, were utilized to verify the simulations carried out with a CFD model ad-hoc setup. After validation, CFD simulations were used to evaluate the effectiveness of the photocatalytic coatings in reducing NO_x concentrations during three time periods representing winter, summer, and transition seasons (spring/autumn) with a focus on the variation of solar radiation/temperature values. As such, besides providing information on the efficacy of the coatings all year-round in Bologna, outputs of this report will also help to extend the results to other European cities characterized by different solar radiation and temperature conditions.</i></p>		
Review status	Action	Person	Date
	Quality Check	Coordination Team	11/02/2019
	Internal Review	Katja Firus (T6 Ecosystems) Achim Drebs (FMI)	11/02/2019
Distribution	Public		

Statement of originality:

This deliverable contains original unpublished work except where clearly indicated otherwise. Acknowledgement of previously published material and of the work of others has been made through appropriate citation, quotation or both.

Revision history			
Version	Date	Modified by	Comments
V0.1	11 Feb 2019	Silvana Di Sabatino, Beatrice Pulvirenti, Erika Brattich, Francesco Barbano, Sara Baldazzi, Francesca Di Nicola, Marco Deserti, Luca Torreggiani, Carla Barbieri, Arianna Trentini, Vanes Poluzzi	Complete first draft to be sent for internal revisions
V0.2	12 Feb 2019	Silvana Di Sabatino, Beatrice Pulvirenti, Erika Brattich	Complete revised version to be checked internally before final submission
V0.3	28 Feb 2019	Beatrice Pulvirenti, Silvana Di Sabatino, Erika Brattich	Final check before final submission
V0.4			

Table of Contents

Table of Contents	4
List of Tables.....	5
List of Figures	5
List of abbreviations.....	7
1. Executive Summary	8
2. Introduction.....	8
3. Methodology	10
3.1 Lazzaretto site	10
3.2 Modeling the photocatalytic coating	11
3.2.1 Equations and models.....	11
3.2.2 Discretization methods and meshes	13
3.2.3 Grid sensitivity tests	14
3.3 Summer	16
3.3.1 Validation of the simulations	16
3.3.2 Results and discussion	17
3.4 Winter and transition seasons	29
3.4.1 Winter case: 04/01/2018, 12:00 UTC.....	29
3.4.2 Transition season case: 17/04/2018, 12:00 UTC.....	31
3.4.3 Comparison between the three cases.....	32
4. Conclusions	33
5. References / Bibliography	34

List of Tables

TABLE 1. OVERVIEW OF THE CFD SIMULATIONS PERFORMED IN THIS WORK: PERIOD OF THE YEAR AND PURPOSE.	10
TABLE 2. WIND DIRECTION AND VELOCITY, FRICTION VELOCITY (U_*) AND ROUGHNESS LENGTH REPRESENTATIVE FOR THE TERRAIN WINDWARD THE COMPUTATIONAL DOMAIN (Z_0) DATA USED FOR SETTING THE BOUNDARY CONDITIONS IN THE LAZZARETTO SITE CASES DURING THE SUMMER 2018 EXPERIMENTAL CAMPAIGN.	13
TABLE 3. MEASURED TEMPERATURE DATA USED FOR SETTING THE BOUNDARY CONDITIONS IN THE LAZZARETTO SITE CASES (A AND B CANYONS, RESPECTIVELY INDICATED AS TA AND TB) DURING THE SUMMER 2018 EXPERIMENTAL CAMPAIGN.	13
TABLE 4. SOME OF THE GRIDS USED FOR THE SENSITIVITY TESTS. THE BOX DIMENSION IS INDICATED AS A FUNCTION OF H, WHERE H STANDS FOR CANYON HEIGHT; S_{MIN} IS THE MINIMUM CELL CHARACTERISTIC SIZE.	15
TABLE 5. COMPARISON BETWEEN NO CONCENTRATIONS OBTAINED FROM THE EXPERIMENTS AND FROM THE SIMULATIONS	17
TABLE 6. WIND AND TEMPERATURE (AIR, WALLS AND STREET) DATA USED FOR SETTING THE BOUNDARY CONDITIONS IN THE WINTER AND SPRING CASES.	29

List of Figures

FIGURE 1. OVERVIEW OF LAZZARETTO SITE AND SURROUNDING AREA (LEFT) AND THE TWO STREET CANYONS (RIGHT). ..	10
FIGURE 2. LAZZARETTO SITE. MESH ON THE BUILDING SURFACES (LEFT TOP), ELEVATION OF THE BUILDINGS (RIGHT, TOP), TOP VIEW OF THE MESH (LEFT, BOTTOM) AND THE COMPUTATIONAL DOMAIN (RIGHT, BOTTOM).	14
FIGURE 3. EXAMPLE OF MESH ZONES (LEFT) AND GRID REFINEMENT NEAR WALLS (RIGHT).	15
FIGURE 4. CONVERGENCE TESTS RESULTS REPRESENTED AS NORMALIZED ROOT MEAN SQUARE ERROR AS A FUNCTION OF NUMBER OF CELLS FOR WIND VELOCITY, NO CONCENTRATION, AND TEMPERATURE.	16
FIGURE 5. ORIENTATION OF THE DOMAIN FOR CASE 1: 17/08/2018, AT 2:00 UTC.	18
FIGURE 6. STREAMLINES OBTAINED FOR CASE 1: 17/08/2018, 2:00 UTC.	18
FIGURE 7. 3D CONTOURS OF NO MOLAR CONCENTRATION (KMOL/M^3 ; $1 \text{ KMOL/M}^3 = 30 \cdot 10^9 \text{ MG/M}^3$) OBTAINED FOR CASE 1: 17/08/2018, 2:00 UTC.	19
FIGURE 8. CANYON A. STREAMLINES (LEFT) AND 3D CONTOURS OF NO MOLAR CONCENTRATION (KMOL/M^3 ; $1 \text{ KMOL/M}^3 = 30 \cdot 10^9 \text{ MG/M}^3$) (RIGHT) OBTAINED FOR CASE 1: 17/08/2018, 2:00 UTC.	19
FIGURE 9. CANYON A. LAYER OF CLIMBING IVY AT THE WEST OPENING.	20
FIGURE 10. CANYON A: VELOCITY VECTORS IN A VERTICAL PLANE NEAR THE SOURCE FOR CASE 1: 17/08/2018, 2:00 UTC.	20
FIGURE 11. CANYON B: 2D CONTOURS OF NO MOLAR CONCENTRATION (KMOL M^{-3} ; $1 \text{ KMOL/M}^3 = 30 \cdot 10^9 \text{ MG/M}^3$) OBTAINED FOR CANYON A ON A VERTICAL PLANE INTERSECTING THE SOURCE (LEFT) AND VELOCITY VECTORS IN IN THE SAME PLANE FOR CASE 1: 17/08/2018, 2:00 UTC.	21
FIGURE 12. ORIENTATION OF THE DOMAIN FOR CASE 2: 17/08/2018, 11:00 UTC.	21
FIGURE 13. STREAMLINES OBTAINED FOR CASE 2: 17/08/2018, 11:00 UTC.	22
FIGURE 14. 3D CONTOURS OF NO MOLAR CONCENTRATION (KMOL M^{-3} ; $1 \text{ KMOL/M}^3 = 30 \cdot 10^9 \text{ MG/M}^3$) OBTAINED FOR CASE 2: 17/08/2018, 11:00 UTC.	22
FIGURE 15. CANYON A. STREAMLINES (LEFT) AND 3D CONTOURS OF NO MOLAR CONCENTRATION (KMOL M^{-3} ; $1 \text{ KMOL/M}^3 = 30 \cdot 10^9 \text{ MG/M}^3$) (RIGHT) OBTAINED FOR CASE 2: 17/08/2018, 11:00 UTC.	23
FIGURE 16. CANYON A: CONTOURS OF NO MOLAR CONCENTRATION (KMOL M^{-3} ; $1 \text{ KMOL/M}^3 = 30 \cdot 10^9 \text{ MG/M}^3$) OBTAINED FOR CASE 1: 17/08/2018, 11:00 UTC. LEFT: PC ABSORPTION IS NOT ACTIVATED, RIGHT PC ABSORPTION IS ACTIVATED.	23
FIGURE 17. CANYON A: CONTOURS OF NO MOLAR CONCENTRATION (KMOL M^{-3} ; $1 \text{ KMOL/M}^3 = 30 \cdot 10^9 \text{ MG/M}^3$) OBTAINED FOR CASE 1: 17/08/2018, 11:00 UTC AT THE NORTH WALL (TOP) AND AT THE SOUTH WALL (BOTTOM). LEFT: PC ABSORPTION IS NOT ACTIVATED, RIGHT: PC ABSORPTION IS ACTIVATED.	24
FIGURE 18. CANYON B: 2D CONTOURS OF NO MOLAR CONCENTRATION (KMOL M^{-3} ; $1 \text{ KMOL/M}^3 = 30 \cdot 10^9 \text{ MG/M}^3$) OBTAINED FOR CANYON A ON A VERTICAL PLANE INTERSECTING THE SOURCE (LEFT) AND VELOCITY VECTORS IN IN THE SAME PLANE FOR CASE 2: 17/08/2018, 11:00 UTC.	24

FIGURE 19. ORIENTATION OF THE DOMAIN FOR CASE 3: 17/08/2018, 14:00 UTC.....	25
FIGURE 20. STREAMLINES OBTAINED FOR CASE 3: 17/08/2018, 14:00 UTC.	25
FIGURE 21. 3D CONTOURS OF NO MOLAR CONCENTRATION (KMOL M^{-3} ; $1 \text{ KMOL/M}^3 = 30 \cdot 10^9 \text{ MG/M}^3$) OBTAINED FOR CASE 3: 17/08/2018, 14:00 UTC 14.	26
FIGURE 22. CANYON A. STREAMLINES (LEFT) AND 3D CONTOURS OF NO MOLAR CONCENTRATION (KMOL M^{-3} ; $1 \text{ KMOL/M}^3 = 30 \cdot 10^9 \text{ MG/M}^3$) (RIGHT) OBTAINED FOR CASE 2: 17/08/2018, 14:00 UTC.....	26
FIGURE 23. CANYON A: CONTOURS OF NO MOLAR CONCENTRATION (KMOL M^{-3} ; $1 \text{ KMOL/M}^3 = 30 \cdot 10^9 \text{ MG/M}^3$) OBTAINED FOR CASE 3: 17/08/2018, 14:00 UTC. LEFT: PC ABSORPTION IS NOT ACTIVATED; RIGHT: PC ABSORPTION IS ACTIVATED.	27
FIGURE 24. CANYON A: CONTOURS OF NO MOLAR CONCENTRATION (KMOL M^{-3} ; $1 \text{ KMOL/M}^3 = 30 \cdot 10^9 \text{ MG/M}^3$) OBTAINED FOR CASE 2: 17/08/2018, 14:00 AT THE NORTH WALL (TOP) AND AT SOUTH WALL (BOTTOM). LEFT: PC ABSORPTION IS NOT ACTIVATED; RIGHT: PC ABSORPTION IS ACTIVATED	28
FIGURE 25. CANYON A: PROFILES OF NO MASS CONCENTRATION ($\mu\text{G M}^{-3}$) OBTAINED FOR CASE 3: 17/08/2018, 14:00 UTC. LEFT: PROFILES OF NO MASS CONCENTRATION ($\mu\text{G M}^{-3}$) AT A DISTANCE OF 25 CM FROM THE NORTH WALL; RIGHT: NO CONCENTRATION PROFILE AT 50CM DISTANCE FROM THE NORTH WALL.	28
FIGURE 26. CANYON B: 2D CONTOURS OF NO MOLAR CONCENTRATION (KMOL M^{-3} ; $1 \text{ KMOL/M}^3 = 30 \cdot 10^9 \text{ MG/M}^3$) OBTAINED FOR CANYON A ON A VERTICAL PLANE INTERSECTING THE SOURCE (LEFT) AND VELOCITY VECTORS IN IN THE SAME PLANE (RIGHT) FOR CASE 3: 17/08/2018, 14:00 UTC.	28
FIGURE 27. CANYON A. STREAMLINES OBTAINED FOR CASE 04/01/2018, 12:00 UTC.	30
FIGURE 28. CANYON A. 3D CONTOURS OF NO MOLAR CONCENTRATION (KMOL M^{-3} ; $1 \text{ KMOL/M}^3 = 30 \cdot 10^9 \text{ MG/M}^3$) OBTAINED FOR CASE 04/01/2018, 12:00 UTC.	30
FIGURE 29. 2D CONTOURS OF NO MOLAR CONCENTRATION (KMOL M^{-3} ; $1 \text{ KMOL/M}^3 = 30 \cdot 10^9 \text{ MG/M}^3$) OBTAINED FOR CANYON A (LEFT) AND B (RIGHT) ON A VERTICAL PLANE NEAR THE SOURCE FOR CASE 04/01/2018, 12:00 UTC.	31
FIGURE 30. CANYON A. STREAMLINES OBTAINED FOR CASE 17/04/2018, 12:00 UTC.	31
FIGURE 31. CANYON A. 3D CONTOURS OF NO MOLAR CONCENTRATION (KMOL M^{-3} ; $1 \text{ KMOL/M}^3 = 30 \cdot 10^9 \text{ MG/M}^3$) OBTAINED FOR CASE 17/04/2018, 12:00 UTC.	32
FIGURE 32. 2D CONTOURS OF NO MOLAR CONCENTRATION (KMOL M^{-3} ; $1 \text{ KMOL/M}^3 = 30 \cdot 10^9 \text{ MG/M}^3$) OBTAINED FOR CANYON A (LEFT) AND B (RIGHT) ON A VERTICAL PLANE NEAR THE SOURCE FOR CASE 17/04/2018, 12:00 UTC.	32
FIGURE 33. CANYON A: PROFILES OF NO MASS CONCENTRATION ($\mu\text{G M}^{-3}$) OBTAINED FOR CASES: SUMMER (17/08/2018, 14:00 UTC), WINTER (04/01/2018) AND SPRING (17/04/2018). LEFT: PROFILES OF NO MASS CONCENTRATION ($\mu\text{G M}^{-3}$) AT 25CM DISTANCE FROM THE NORTH WALL: RIGHT: NO CONCENTRATION PROFILE AT 50CM DISTANCE FROM THE NORTH WALL.....	33

List of abbreviations

ARPAE:	Regional Environmental Protection Agency of Emilia Romagna
CFD:	Computational Fluid Dynamics
D:	Deliverable
EEA:	European Environment Agency
EMEP:	European Monitoring and Evaluation Programme
GI:	Green Infrastructure
H:	Height
IR:	InfraRed
ISPRA:	Istituto Superiore per la Protezione e la Ricerca Ambientale
LBW:	Low Boundary Wall
NO _x :	Nitrogen Oxides
NO:	Nitric Oxide
OC:	Organic Substances
O ₃ :	Ozone
PC:	PhotoCatalytic
PCS:	Passive Control System
PM:	Particulate Matter
RANS:	Reynolds-Averaged Navier-Stokes
SO ₂ :	Sulfur Dioxide
SO _x :	Sulfur Oxides
UTC:	Coordinated Universal Time
UV:	UltraViolet
W:	Width

1. Executive Summary

This report aims to detail the functionality and effectiveness of photocatalytic coating over three representative annual periods. While the assessment of the photocatalytic coatings in reducing NO_x concentrations in urban street canyons under summer weather conditions was tested and verified within an intensive experimental campaign performed in the Lazzaretto area located in the Municipality of Bologna, thoroughly described in D3.8, the aim of this Deliverable is to detail and generalize those results taking into account the different weather conditions which can affect the area all over the area.

In this case, the analysis entirely depends on the results of model simulations, validated comparing the output of numerical simulations with the experimental data gathered and described within the summer experimental campaign. Simulations thus assess the effectiveness of the physical intervention depending on the different weather conditions along the year. In particular, here, the focus was restricted on the dependence on the different solar radiation and temperature values along the seasons was evaluated, whereas the wind direction was kept fixed. The results of the validated numerical simulations have shown potential reductions of 40-50% near the painted walls, i.e. higher than those measured within the experiments. In addition, notwithstanding the lower winter solar radiation and temperature, winter reductions at noon can be even higher than those observed during summer afternoons, when some walls are in the shadows. As such, besides providing information on the efficacy of the coatings all year-round in Bologna, outputs of this report will also help to extend the results to other European cities characterized by different solar radiation and temperature conditions.

2. Introduction

Among the passive techniques whose effectiveness and functionality are tested in the iSCAPE project, photocatalysis was introduced quite recently with the aim to transform harmful substances for human health into inert salts not directly affecting human respiration (D1.2). In particular titanium oxide compounds (TiO_2), activated by UV solar radiation, react with the nitrogen oxides (NO_x), sulfur oxides (SO_x) and organic substances (OC) present in air, also in the form of atmospheric particulate matter (PM), producing inert particles that adhere to the wall to which the coatings have been applied. The physical mechanism on the basis of this technique is like that of photosynthesis: the UV radiation acts on the coating layer, generating electron-hole pairs, which in turn generate very reactive free radicals (OH), which combine with the pollutants transforming them into inert particles such as nitrates sodium (NaNO_3) or calcium nitrate ($\text{Ca}_2(\text{NO}_3)_2$). Although the use of photocatalytic coatings (PC) in the real atmosphere is still in the experimental phase and the scientific literature on the subject has not yet reached a consensus, these paints have been extensively tested in the laboratory, showing that they can produce up to 50% absorption of the NO_x they are in contact with (Mills, 2007). Furthermore, the reactions can also occur with nanometric or micrometric particles (Folli et al., 2010).

Few experiments are available in the literature on the effectiveness of photocatalytic paints conducted outdoors, in the street.

An experiment to evaluate the application of interior paints, therefore in places with little availability of UV rays was conducted inside the Umberto I tunnel, in the center of Rome, Italy (Guerrini et al., 2012). The location was chosen by virtue of the relative low variety of elements acting. Main parameters to be considered are the flow of air and of the vehicles that pass through the tunnel. The measurements, compared with the reference data measured at official air quality stations of the city of Rome by the Environmental Protection Agency near the tunnel, showed a reduction of NO_x exceeding 20%, with peaks of over 50% during the summer, when the availability of UV rays also increases at the entrance

to the tunnel. Furthermore, the peaks related to all NO_x species, measured outside the tunnel, have not been recorded internally.

Gallus et al. (2015) measured the effects of photocatalytic cementitious coating materials applied on the side walls and ceiling of a tunnel in Brussels, Belgium (the Leopold II tunnel). They monitored the pollutant before and after the application of the photocatalytic coating. After the application, they monitored the pollutants at the same time at two measurement sites up-wind and down-wind of the tunnel, activated by UV lamps. In this case, they found a photocatalytic NO_x reduction lower than 2%. From laboratory analysis, they found that the photocatalytic material showed a serious deactivation under the heavily polluted tunnel conditions. Moreover, the UVA irradiance given by the lamps was below the targeted values.

Ballari and Browers (2013) performed full-scale measurements on a street in Hengelo, The Netherlands (Castorweg street). Concrete pavement blocks, added with photocatalytic material TiO_2 based were substituted in half of the street, called De NO_x street, while the other half was covered by untreated blocks. They compared the NO_x measurements made in the De NO_x street with those made in the control street during few days in summer and autumn. They found that the NO_x reduction in the De NO_x street was dependent of the weather conditions, with peaks of 28% soon after the photocatalytic material application.

Maggos et al. (2008) measured the photocatalytic properties of a construction material under real environmental conditions but controlled pollution within street canyons build ad hoc in order to give a real scale laboratory test. They built three parallel artificial street canyons, of which one was treated with photocatalytic material. They measured NO_x concentrations in the treated street canyon and compared with the measures in the reference canyon, during summer. They found reductions in the range 36.7-82%, depending on the wind direction. These differences were measured very close to the canyon walls (15-30 cm).

Very few works are available in the literature regarding the modeling of the effect of photocatalytic coatings at a field scale. Jeanjean et al. (2017) compared the effect of different pollutant mitigation measures, including photocatalytic coatings, by means of a CFD approach. They modelled the NO_x removal action of photocatalytic coatings by means of a deposition model similar to the one used for modeling the pollutant deposition on plants, without validation. They compared different scenarios by applying the model to a real street in London (Oxford street) with different pollutant mitigation measures, showing that photocatalytic coatings on building surfaces present minimal improvement to overall air quality. However, they showed that photocatalytic coatings can significantly lower NO_x concentrations in street canyons near the hotspots, depending on the street geometry and its orientation with respect to the wind direction.

In this report a CFD-based approach to model the effect of photocatalytic coatings on the local distribution of NO concentration within a real street canyon is tackled. The model is firstly applied to the Lazzaretto site in Bologna during August 2018, i.e. during the period of the summer 2018 experimental campaign in the Lazzaretto area, thoroughly described in D3.8. In particular, two parallel street canyons in the area have been identified, where an intensive experimental field campaign with an instrumentation setup similar to the one previously used within the two summer 2017 and winter 2018 experimental campaigns in Bologna (D3.3 and D5.2) was adopted, with the aim to assess the effectiveness of the photocatalytic coatings in reducing NO_x concentrations in urban street canyons. Briefly, two ARPAE (previously, ARPA-ER) mobile laboratories for the measurements of air quality pollutants were deployed in each street canyon, while measurements of meteorological and turbulence variables at fast time resolution were performed at two different height levels (i.e., inside and above the two canyons). After one week of contemporary measurements to compare the intrinsic differences of the two canyons, one of the two canyons was painted with the photocatalytic coatings, while the other, to be used as a reference, was left untouched. During the campaign, a few (total of 8) controlled pollutant releases with

a known pollution source (one EURO-2 diesel car) have been performed (D3.8). Within the experimental campaign in August 2018, NO_x pollutant concentrations have been measured in both canyons by two ARPAE mobile laboratories. Measurements conducted within the experimental campaign served to compare the numerical results and to set a calibration and a verification of the simulation of pollutant reduction at the wall. After the verification, here the model has been applied to other meteorological conditions representative of winter and transition seasons, to evaluate the effectiveness of the coatings over different meteorological conditions along the year (Table 1).

Season	Case	Purpose
Summer	17/08/2018, night	Validation without PC activation
Summer	17/08/2018, day	Verification of the setup; evaluation of the PC effect
Summer	17/08/2018, day	Final validation of the simulation with PC activation; evaluation of the PC effectiveness under summer conditions
Winter	04/01/2018, day	Evaluation of the PC effectiveness under winter conditions
Transition (spring)	17/04/2018, day	Evaluation of the PC effectiveness under spring conditions

Table 1. Overview of the CFD simulations performed in this work: period of the year and purpose.

3. Methodology

3.1 Lazzaretto site

Lazzaretto area is a neighborhood of the Municipality of Bologna located outside the city center. It is characterized by a major street (Terracini street), with smaller alleys on the east side. These streets are within a University Campus, with a low packing building density. An overview of the study area is shown in Figure 1. The campus is characterized by streets with low traffic, but the streets around the campus are characterized by intense car traffic. Two street canyons within the campus (called A and B) have been considered in the experimental campaign described in D3.8, with aspect ratios $H/W(A)=1.68$ and $H/W(B)=0.89$. The streets canyons orientation with respect to the North-South coordinate is 145°.



Figure 1. Overview of Lazzaretto site and surrounding area (left) and the two street canyons (right).

3.2 Modeling the photocatalytic coating

3.2.1 Equations and models

The Computational Fluid Dynamics code CD-adapco STAR-CCM+ 12.02.10 (Siemens) has been employed to solve the steady-state RANS (Reynolds-Averaged Navier-Stokes) equations with realizable k - ε turbulence model. The buoyancy thermal effects have been considered in this work.

The transport equations for kinetic energy k and the turbulent dissipation rate ε are:

$$\frac{\partial}{\partial t}(\rho k) + \nabla \cdot (\rho k u) = \nabla \cdot \left[\left(\mu + \frac{\mu_t}{\sigma_k} \right) \nabla k \right] + P_k - \rho(\varepsilon - \varepsilon_0) + S_k \quad (1)$$

and

$$\frac{\partial}{\partial t}(\rho \varepsilon) + \nabla \cdot (\rho \varepsilon u) = \nabla \cdot \left[\left(\mu + \frac{\mu_t}{\sigma_\varepsilon} \right) \nabla \varepsilon \right] + \frac{1}{T_e} C_{\varepsilon 1} P_\varepsilon - C_{\varepsilon 2} f_2 \rho \left(\frac{\varepsilon}{T_e} - \frac{\varepsilon_0}{T_0} \right) + S_\varepsilon \quad (2)$$

where u is the average velocity, μ is air dynamic viscosity, σ_k , σ_ε , $C_{\varepsilon 1}$, $C_{\varepsilon 2}$ are model coefficients, P_k and P_ε are production terms, whose formulation depends on the k - ε model variant, f_2 is a damping function that mimics the decrease of turbulent mixing near the walls, enforcing realizability, S_k and S_ε are used specific source terms, ε_0 is the ambient turbulent dissipation rate value in the source terms, T_e is the large-eddy time scale, T_0 the specific time-scale related to ambient turbulent source term.

Mean flow, turbulence, energy and dispersion equations were discretized using a second order schemes and the SIMPLE scheme was used for pressure-velocity coupling.

3.2.1.1 Heat transfer model

The buoyancy forces have been considered under the following approximation, i.e. in Navier-Stokes equation the density ρ is assumed to be a function of temperature and pressure in accordance with the ideal gas law

$$\rho(T, p) = \frac{p}{RT} \quad (3)$$

where R is the specific gas constant, $R = \frac{R_0}{M}$, with $R_0 = 8314.4621$ (J kmol K⁻¹) and M is the gas molecular weight.

3.2.1.2 Species transport model

The model of NO mass diffusion equation is:

$$J = - \left(\rho D + \frac{\mu_t}{Sc_t} \right) \nabla c \quad (4)$$

where c is NO mass fraction, D is the molecular diffusion coefficient, μ_t is the turbulent viscosity, $Sc_t = 0.7$ is the turbulent Schmidt number.

The pollutant source has been simulated by separating volumes with dimension 0.5 m x 0.5 m x 0.5 m in the middle of the canyon. A controlled pollutant releases with a known pollution source (one EURO-2 diesel car) has been setup in each of the two street canyons. The emission rate was set using ISPRA

(Istituto Superiore per la Protezione e la Ricerca Ambientale)¹ emission factors, based on EMEP/EEA (European Monitoring and Evaluation Programme/European Environment Agency) air pollutant emission inventory (EEA, 2016), for EURO-2 diesel car (0.63 g/km total NO emission, increased of 50% to take into account the increase in emissions with mileage).

3.2.1.3 Modelling of the photocatalytic absorption by the walls

The pollutant flux S_d (g m⁻² s⁻¹) is calculated as the product of the deposition velocity V_d (cm s⁻¹) and pollutant concentration c (g m⁻³)

$$S_d = -V_d c \quad (5)$$

In order to determine the deposition velocity, the approach similar to the one shown by Staub de Melo and Triches (2012) described as follows.

$$NO_{r,flux} = \frac{NO_r p M \dot{V}}{8131.4 T A} \quad (6)$$

Where NO_r is the maximum NO removal measured by the experiments (ppmv), p is the atmospheric pressure (Pa), M is the molecular mass of NO (g/mol), \dot{V} is the volume flow rate (m³ s⁻¹), T is the temperature (K) and A is the area painted with photocatalytic coatings.

3.2.1.4 Boundary conditions

The boundary and initial conditions set in the simulations derive from experimental data obtained during a field campaign conducted on August 2018. Meteorological data have been obtained from observations at two ARPAE meteorological stations in different points of the city: the first one, Asinelli station, is a synoptic meteorological station located at the top of Asinelli's tower in Bologna city center, the highest building of the city (96 meters above ground level) and the second one, Silvani station, is a urban meteorological station placed on the roof of ARPAE's headquarter, in a major street in the ring which surrounds Bologna city center (27 meters above ground level).

At the inflow boundary, vertical profiles for mean velocity u , turbulence kinetic energy k and turbulence dissipation rate ε of the neutrally stratified atmospheric boundary layer were imposed according to:

$$u(z) = \frac{u_*}{k} \ln \left(\frac{z+z_0}{z_0} \right) \quad (7)$$

$$k(z) = \frac{u_*^2}{\sqrt{C_\mu}} \left(1 - \frac{z}{\delta} \right) \quad (8)$$

$$\varepsilon(z) = \frac{u_*^3}{kz} \left(1 - \frac{z}{\delta} \right) \quad (9)$$

with z the vertical position above the ground, z_0 the roughness length representative for the terrain windward the computational domain, u_* the friction velocity, $k=0.42$ the van Karman constant, $C_\mu=0.09$ and δ the height of the computational domain.

The inflow wind profile has been calculated solving Eqs. 7-9, using data from the two meteorological stations (Asinelli and Silvani), in order to obtain the friction velocity u_* for every different wind condition (Table 2).

¹ ISPRA, the Italian Institute for Environmental Protection and Research, is a public research institute, with a main function of support to the Environment Ministry and of protection of territory and sea.

The temperature measurements recorded by the monitoring stations have been analyzed to create air temperature profiles: during the day the temperatures do not have a significant variation according to height, therefore constant profiles have been created. During the night of the summer case, thermal inversion occurs at a height of about 100 meters; therefore, the temperature profiles have a constant increase (about 2°C/100 m) until the temperature inversion quota and then a constant decrease 0.7°C/100 m).

Concentration measurements provided by ARPAE's air quality mobile stations and meteorological measurements recorded inside (about half of the canyon height) and over the canyons (top level, over the buildings' roof) stations were used to validate the numerical model.

Day	Time (UTC)	Wind direction (°) and wind velocity (m/s)	u^* (m s ⁻¹)	z_0 (m)
17/08/2018	4:00	218° – 3.4	0.21	0.1
17/08/2018	11:00	319° – 0.9	0.11	0.1
17/08/2018	14:00	8° – 2.8	0.21	0.1

Table 2. Wind direction and velocity, friction velocity (u^*) and roughness length representative for the terrain windward the computational domain (z_0) data used for setting the boundary conditions in the Lazzaretto site cases during the summer 2018 experimental campaign.

For each direction of the wind, a computational grid has been created in order to have the inlet section perpendicular to the wind.

Temperature boundary conditions have been set at the walls of the street canyons and at the street between the buildings. The street canyon façade temperatures have been measured during thermographic campaigns with an IR camera which were performed during the days of the controlled pollutant releases with a methodology similar to that used and thoroughly described in D3.3 and D5.2. In addition, the IR camera was also used to measure the ground temperature and the values obtained from the thermographic images were set into the simulations.

The air temperature was measured by ARPAE van measurement instrumentations and by means of thermohygrometers deployed at the two height levels (as described in D3.8). The results are shown in Table 3.

Day	Time (UTC)	T _{air} (°C)	TA_South (°C)	TA_North (°C)	TA_street (°C)	TB_South (°C)	TB_North (°C)	TB_street (°C)
17/08/2018	4:00	21.0	32.0	31.8	30.1	26.0	29.4	26.9
17/08/2018	11:00	30.4	27.3	28.6	43.7	28.3	30.7	44.4
17/08/2018	14:00	31.1	46.0	36.9	36.3	49.5	34.9	32.5

Table 3. Measured temperature data used for setting the boundary conditions in the Lazzaretto site cases (A and B canyons, respectively indicated as TA and TB) during the summer 2018 experimental campaign.

3.2.2 Discretization methods and meshes

Different meshes with the same constructive approach have been created for the two different street canyons.

The computational domain, shown in Figure 2, has a size of 652 m x 375 m x 130 m.

Symmetry boundary conditions have been assigned to the lateral sides and the domain top, a velocity inlet condition was set to the inlet boundary and a pressure outlet condition to the outflow boundary. A no-slip boundary condition was applied at the ground and at the building surfaces.

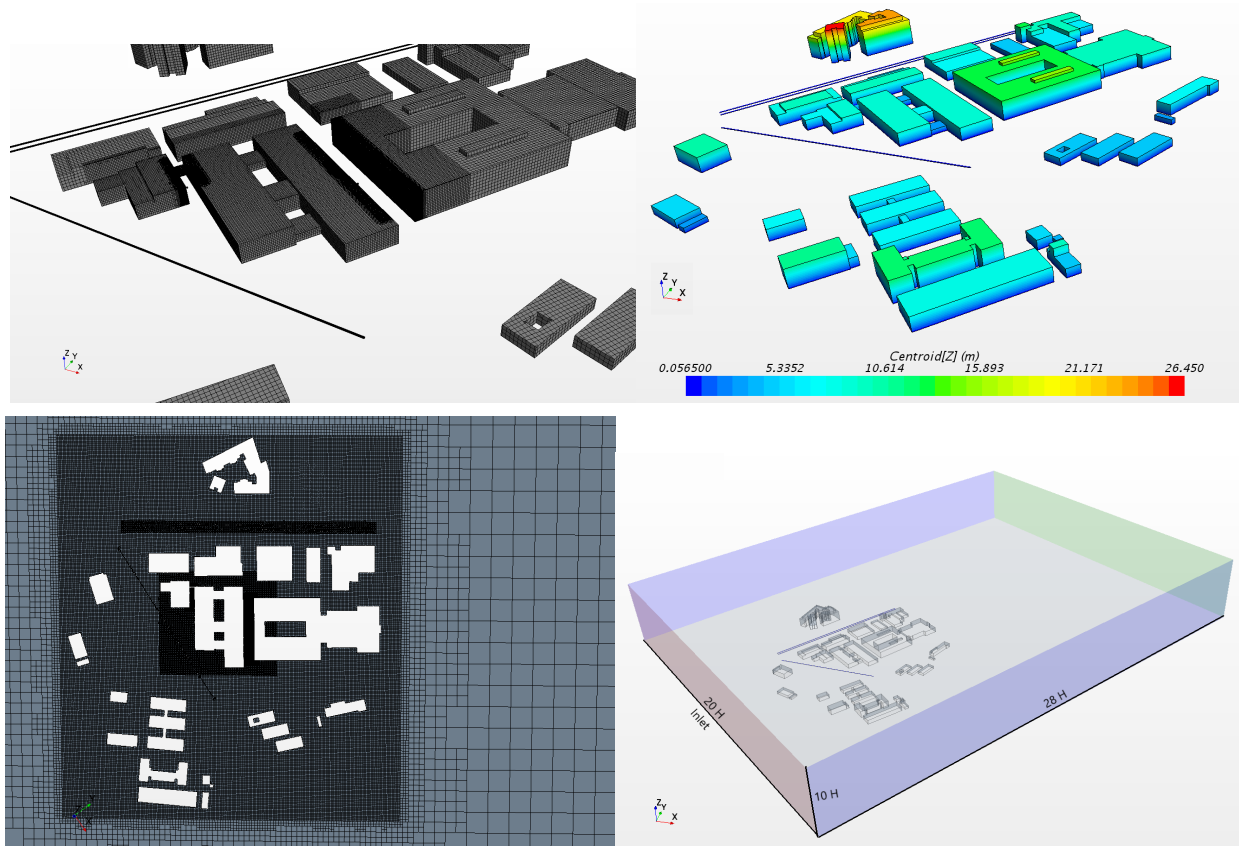


Figure 2. Lazzaretto site. Mesh on the building surfaces (left top), elevation of the buildings (right, top), top view of the mesh (left, bottom) and the computational domain (right, bottom).

3.2.3 Grid sensitivity tests

A set of preliminary sensitivity tests have been performed, both for choosing the dimensions of the boxes used for refinements and for choosing the dimensions of the elements near the building walls. As shown in Figure 3, the mesh is built by three zones, each one characterized by structured elements with homogeneous dimensions. The first zone is the external domain, with the coarsest elements, containing a box with elements with a medium size and another box surrounding the area and the street canyons, containing the finest elements.

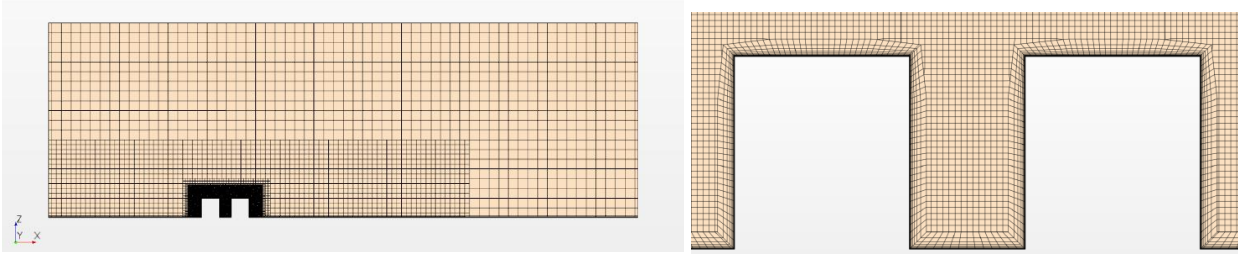


Figure 3. Example of mesh zones (left) and grid refinement near walls (right).

A geometry with a canyon having the same dimensions of canyon A has been used as a base geometry for the first part of the sensitivity tests. Table 4 shows the dimensions of the box containing the finest elements, the size of the elements and the total number of cells N_{cells} in the computational domain. Six refinements have been compared, in the range $N_{cells} = [0.250 - 12.878]$ millions of elements.

Grid name and index	Box dimension	s_{min} (m)	Number of cells (millions)
Very coarse - 5	$2 H$	4.125	0.250
Coarse - 4	$2 \sqrt{2} H$	2.917	0.433
Medium - 3	H	2.062	0.856
Fine - 2	$H/\sqrt{2}$	1.458	1.989
Very fine - 1	$H/2$	1.031	4.855
Ultra-fine - G	$H/2 \sqrt{2}$	0.729	12.878

Table 4. Some of the grids used for the sensitivity tests. The box dimension is indicated as a function of H , where H stands for canyon height; s_{min} is the minimum cell characteristic size.

Figure 4 shows the normalized root mean square deviation obtained from a vertical line in the middle of the canyon, defined as

$$NRMSE_g = \sqrt{\frac{\sum p \left(\frac{x_{g,p} - x_{G,p}}{x_G} \right)^2}{N_p}} \quad (10)$$

where x is the variable used for the comparison (velocity, NO concentration, or temperature), g is the grid number, p is the point along a probe line where the comparison is made, N_p is the number of points in the probe line.

Figure 4 shows that the convergence is achieved for velocity, NO concentration and temperature results.

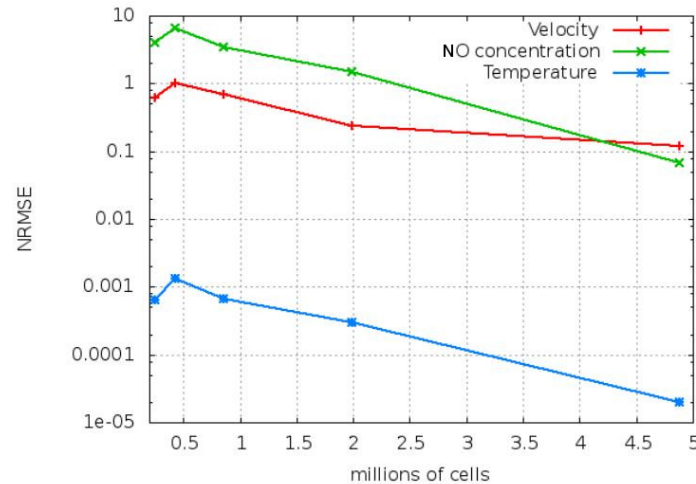


Figure 4. Convergence tests results represented as Normalized Root Mean Square error as a function of number of cells for wind velocity, NO concentration, and temperature.

3.3 Summer

3.3.1 Validation of the simulations

The three cases considered for summer and reported in Table 2 and Table 3 concern two daylight cases (i.e. solar radiation activates the photocatalysis) and one fortnight case (no activation of the photocatalytic coating).

The pollutant source has been simulated by separating a volume with dimensions 0.5 m x 0.5 m x 0.5 m.

In order to determine the deposition velocity and the photocatalytic coating model for the PURETI photocatalytic coatings application at Lazzaretto, the following approach has been set.

A first case with no PC activation has been run (17/08/2018, UTC 4), in order to validate the CFD model in absence of pollutant capturing mechanisms by the walls. Then, one of the two day-time cases has been run (17/08/2018, UTC 11) without activating the photocatalytic effect. A 14% reduction on NO concentrations, in agreement with the experiments (as shown in D3.8), has been applied to the results obtained by this case, to obtain the amount of NO reduction for that case. Then, the NO flux absorbed by the PC activated surfaces has been evaluated, according with Eq. 6.

The value of $NO_{r,flux}$ obtained has been set as a boundary condition at street canyon A (briefly indicated as canyon A in the following) walls, and a run with the same meteorological boundary conditions as the previous case was performed. The results obtained by this simulation have been verified through a comparison with the measurements. From the pollutant concentration obtained at the walls, a value for the deposition velocity has been estimated. Finally, the same value of the deposition velocity obtained from this case has been applied to a third case (17/08/2018, 14:00 UTC) for the final validation. For this last case, the PC effect has been added only to the North wall of the canyon A, as the other wall was in shadow.

The results are provided in Table 5.

Canyon A Canyon A Canyon A Canyon A Canyon B Canyon B

Date	Time (UTC)	Measured NO conc. ($\mu\text{g}/\text{m}^3$)	Simulated NO conc. ($\mu\text{g}/\text{m}^3$) without PC	Simulated NO conc. ($\mu\text{g}/\text{m}^3$) with PC	NO reduction from simulations	Measured NO conc. ($\mu\text{g}/\text{m}^3$)	Simulated NO conc. ($\mu\text{g}/\text{m}^3$)
17/08/2018	4:00	103.3	94.9	-	0	119.3	104.8
17/08/2018	11:00	260.6	305.8	269.5	-11.9%	4.08	6.10
17/08/2018	14:00	59.8	65.7	58.92	-10.3%	5.28	4.56

Table 5. Comparison between NO concentrations obtained from the experiments and from the simulations

Table 5 shows good agreement between measured values and simulations in canyon B (not painted). For canyon A, the simulated NO concentrations without the effect of PC are in agreement with experiments only for the night case, while for the other two cases, the agreement is achieved only when adding the photocatalytic effect on the surfaces. In this case, a reduction of about 12% in the first case (17/08/2018, 12:00 UTC) and a reduction of about 10% in the second case (17/08/2018, 12:00 UTC) was obtained, in good agreement with the results in D3.8 analyzing the measured data.

3.3.2 Results and discussion

3.3.2.1 Case 17/08/2018, 4:00 UTC (night)

This case refers to a night condition, with the walls painted but not active because of the absence of UVA radiation. The boundary conditions for this case are shown in Table 2 and Table 3 (first line, for canyon A). The wind comes from the South-West direction (i.e. the direction of the wind forms an angle of 218° with the North-South direction). In this case, the domain mesh surrounding the buildings has been rotated in order to have the inlet surface perpendicular to the wind direction, as shown in Figure 5.

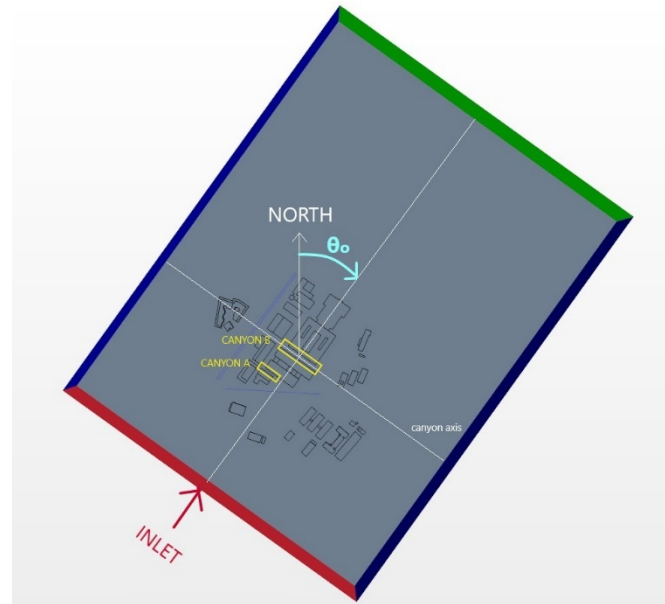


Figure 5. Orientation of the domain for case 1: 17/08/2018, at 2:00 UTC.

In this case, the direction of the wind is almost perpendicular to the canyons, as the canyons axes form an angle of 35° with the North-South direction. Figure 6 shows colored streamlines as a function of the wind velocity obtained for this case. In all the figures, the arrow shows the wind direction.

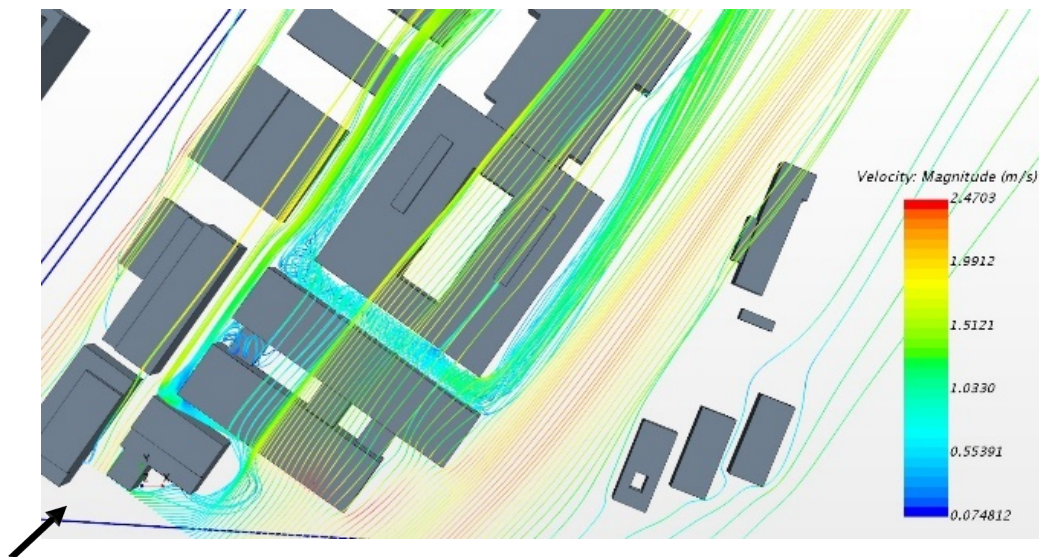


Figure 6. Streamlines obtained for case 1: 17/08/2018, 2:00 UTC.

Figure 6 shows that in canyon B a single vortex is formed, having the typical shape that occurs in street canyons with an aspect ratio close to one when the wind direction is perpendicular to the axis of the canyon. In canyon A, instead, a spiral-shaped vortex is formed, directed along the axis of the canyon towards the North-West exit of the canyon. This vortex is caused by the air that impacts on the East wall out to the canyon (right in the figure) that deviates and enters the canyon, creating that forcing that

deforms the vortex. This difference in the air dynamics creates different plume shapes around the pollutant source, as shown Figure 7. In the two canyons the plumes have different shapes, but also different pollution levels. A focus on the streamlines and the NO plume obtained in canyon A is shown in Figure 8, as seen from the East opening of the canyon.

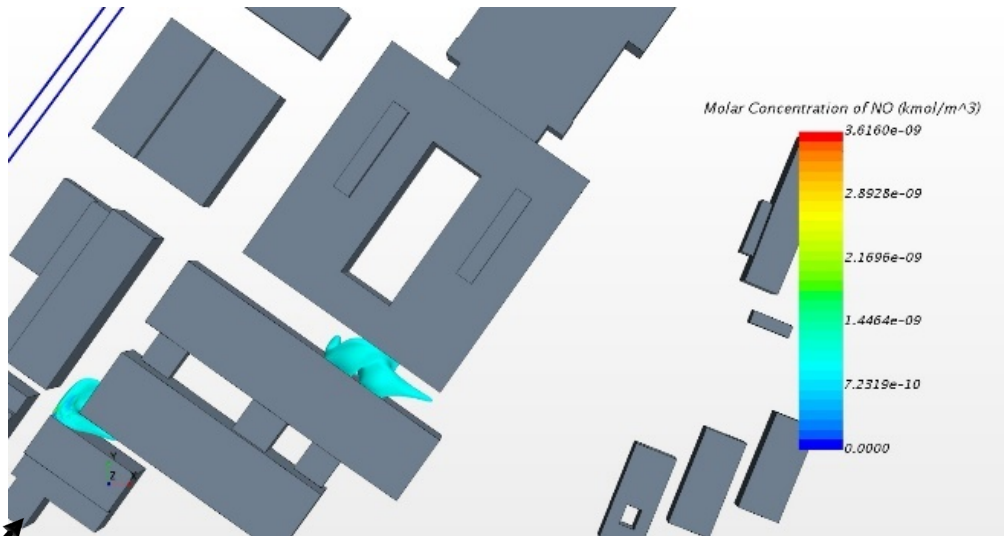


Figure 7. 3D contours of NO molar concentration (kmol/m^3 ; $1 \text{ kmol/m}^3 = 30 \cdot 10^9 \mu\text{g/m}^3$) obtained for case 1: 17/08/2018, 2:00 UTC.

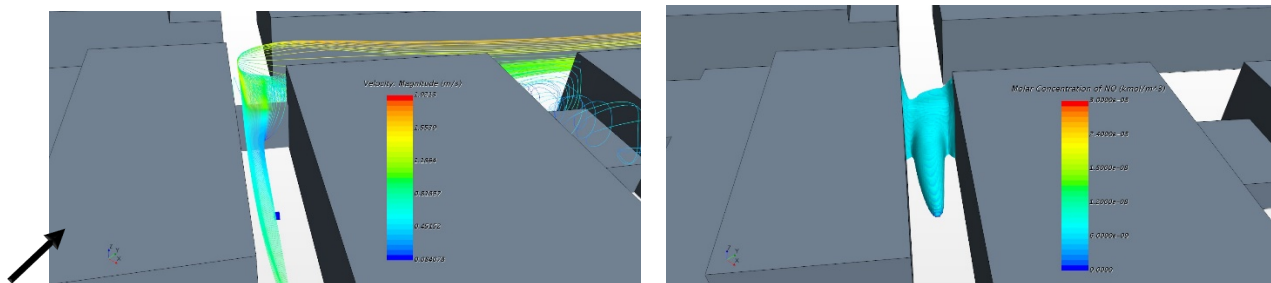


Figure 8. Canyon A. Streamlines (left) and 3D contours of NO molar concentration (kmol/m^3 ; $1 \text{ kmol/m}^3 = 30 \cdot 10^9 \mu\text{g/m}^3$) (right) obtained for case 1: 17/08/2018, 2:00 UTC.

On the West side of the canyon A, as shown by Figure 9, the lower part of the canyon is blocked by a layer of climbing ivy, that forms a permeable obstacle to the flow. This has been taken into account by adding to the geometry a porous wall, with the same numerical approach as that adopted for green infrastructure (GI) described in D6.2. The presence of this GI creates a stagnation in the zone between the source and the West exit of the canyon A, as shown in Figure 8.



Figure 9. Canyon A. Layer of climbing ivy at the West opening.

Figure 10 shows the pollutant concentration on a vertical plane near the source (left) and the velocity vectors on the same plane (right), for **canyon A**. A main air flow, perpendicular to the canyon, drives the pollutant in the direction perpendicular to the plane shown in the figure.

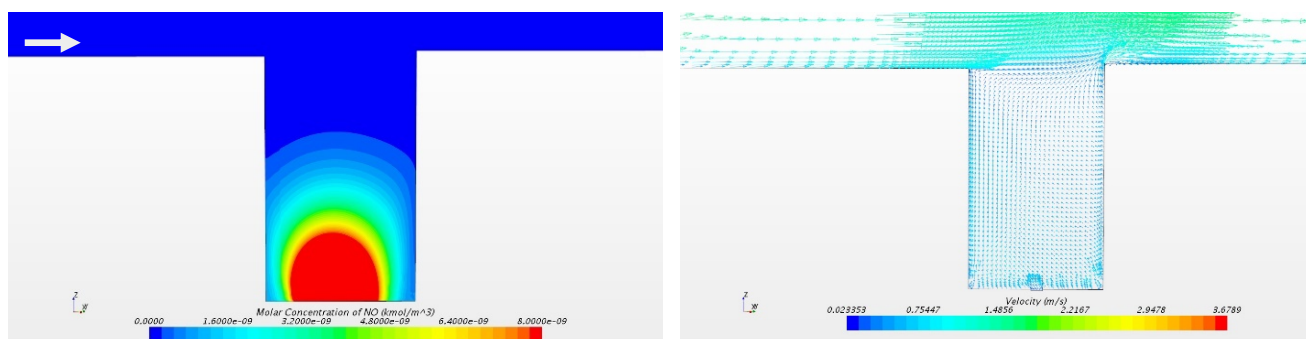


Figure 10. Canyon A: velocity vectors in a vertical plane near the source for case 1: 17/08/2018, 2:00 UTC.

Figure 11 shows the pollutant concentration on a vertical plane near the source (left) and the velocity vectors on the same plane (right), for **canyon B**. A clockwise vortex that occupies the canyon drives the pollutant toward the South wall, where the ARPAE monitoring station was placed.

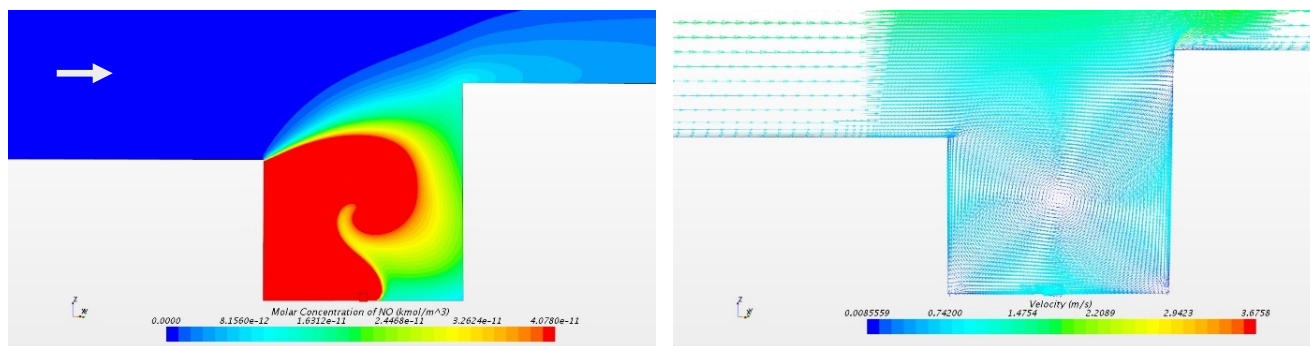


Figure 11. Canyon B: 2D contours of NO molar concentration (kmol m^{-3} ; $1 \text{ kmol/m}^3 = 30 \cdot 10^9 \mu\text{g/m}^3$) obtained for canyon A on a vertical plane intersecting the source (left) and velocity vectors in the same plane for case 1: 17/08/2018, 2:00 UTC

3.3.2.2 Case 17/08/2018, 11:00 UTC

This case refers to a day condition, with the canyon A walls painted and activated from the sun UV radiation. The boundary conditions for this case are provided in Table 2 and Table 3 (second line). The wind comes from the West direction (i.e. the direction of the wind forms and angle of 319° with the north-south direction). The domain mesh surrounding the buildings has been rotated in order to have the inlet surface perpendicular to the wind direction, as shown in Figure 12.

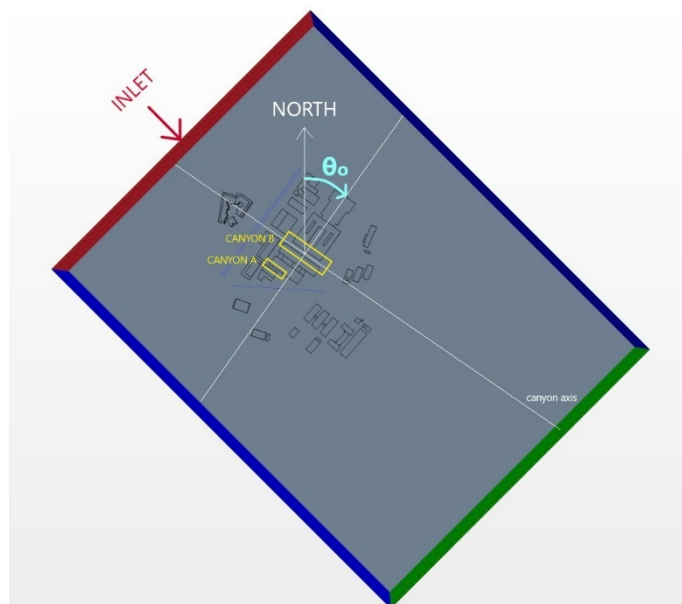


Figure 12. Orientation of the domain for case 2: 17/08/2018, 11:00 UTC.

In this case, the direction of the wind is almost parallel to the canyons, as the canyons axes form an angle of 35° with the direction North-South. Figure 13 shows the streamlines colored as a function of the wind velocity obtained for this case.

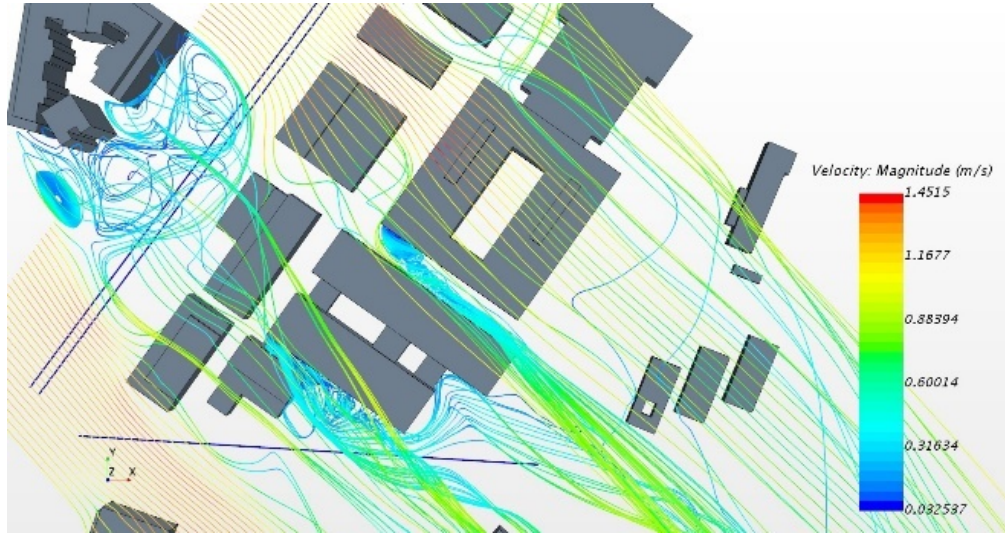


Figure 13. Streamlines obtained for case 2: 17/08/2018, 11:00 UTC.

In this case, the wind coming from North-East creates a wake flow downstream of a group of buildings located just North-east from the campus. The smoothed flow then propagates into the canyon A, where a screwed vortex is formed with very low speed, directed from North-West to South-East. The canyon B is less exposed to the wake flow downstream of the buildings, then the flow is parallel to the axis of the canyon where a vortex is formed, like the one formed in canyon A, but with opposite rotation. Figure 14 shows that both the plumes are directed towards South-East, but in canyon A the plume is pushed toward the North wall, while in canyon B the plume is pushed toward the South wall.

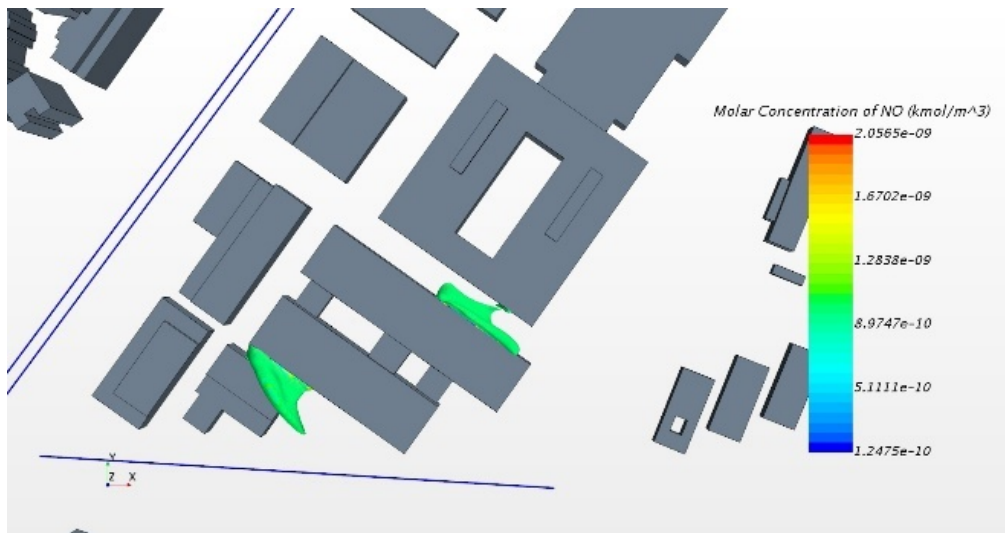


Figure 14. 3D contours of NO molar concentration (kmol m^{-3} ; $1 \text{ kmol/m}^3 = 30 \cdot 10^9 \mu\text{g/m}^3$) obtained for case 2: 17/08/2018, 11:00 UTC.

A zoom of streamlines and plume in the **canyon A** is presented in Figure 15. The dynamics of the flow in this case is more complex. Two vortices are present in the West part of the canyon, one near the street, with axis parallel to the canyon and one in the upper part of the canyon, with axis perpendicular

to the canyon axis. The upper vortex drives the polluted air toward the North wall of the canyon and to the top of the canyon, as shown in Figure 15 (right).

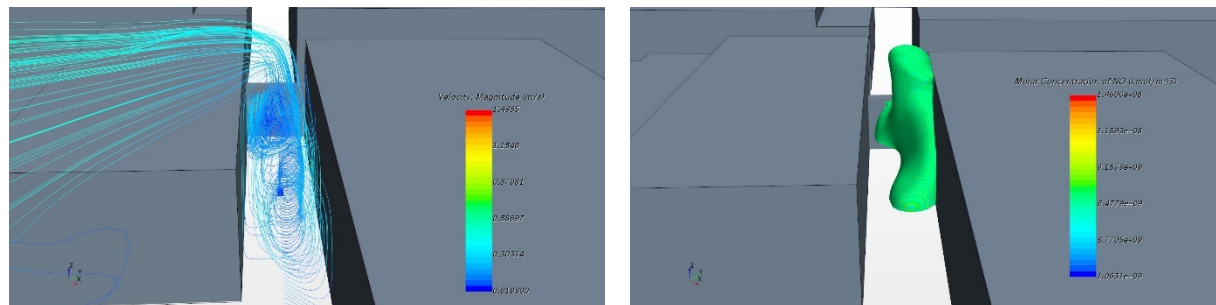


Figure 15. Canyon A. Streamlines (left) and 3D contours of NO molar concentration (kmol m^{-3} ; $1 \text{ kmol/m}^3 = 30 \cdot 10^9 \mu\text{g/m}^3$) (right) obtained for case 2: 17/08/2018, 11:00 UTC.

The presence of these vortices right near the source gives the pollutant concentration distribution shown in Figure 16 on a vertical plane. In the figure, a comparison between the case with no photocatalytic effect (left) and the case where the photocatalytic effect has been activated (right) is shown. A reduction of NO concentration is observed in the region close to the painted surfaces (canyon walls and street), as expected. In fact, this case has been used as a reference for determining the pollutant flux at the walls, according to Eqs. 5 and 6. Figure 17 shows the pollutant concentration obtained on the North and South walls of canyon A in the case of activated photocatalytic effect. From this distribution, a value of the deposition velocity $V_d = 0.37 \text{ cm/s}$ has been obtained and used for the other cases.

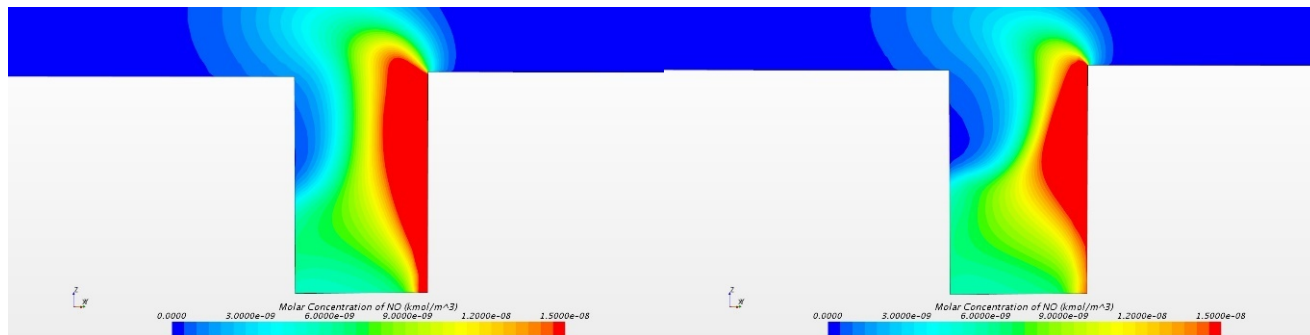
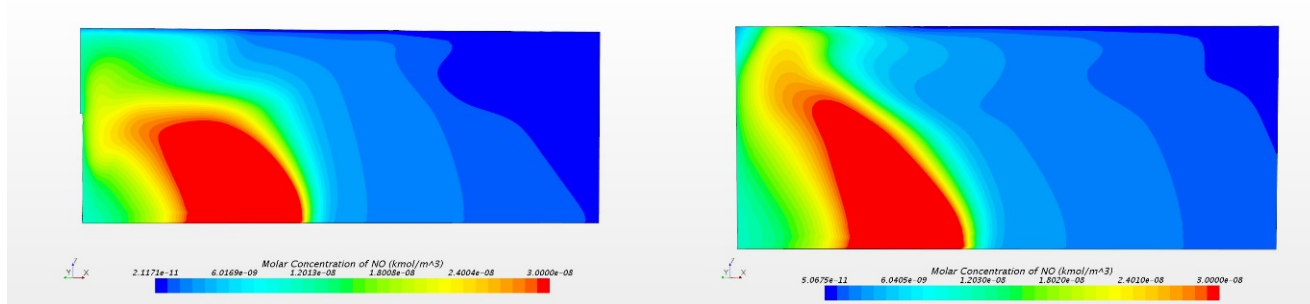


Figure 16. Canyon A: contours of NO molar concentration (kmol m^{-3} ; $1 \text{ kmol/m}^3 = 30 \cdot 10^9 \mu\text{g/m}^3$) obtained for case 1: 17/08/2018, 11:00 UTC. Left: PC absorption is not activated, right PC absorption is activated



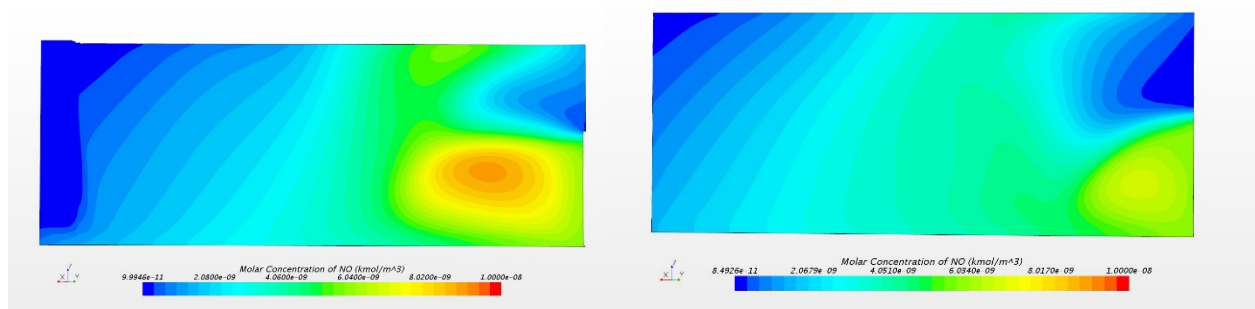


Figure 17. Canyon A: contours of NO molar concentration (kmol m^{-3} ; $1 \text{ kmol/m}^3 = 30 \cdot 10^9 \mu\text{g/m}^3$) obtained for case 1: 17/08/2018, 11:00 UTC at the North wall (top) and at the South wall (bottom). Left: PC absorption is not activated, right: PC absorption is activated.

Finally, Figure 17 shows the pollutant concentration on a vertical plane near the source (left) and the velocity vectors on the same plane (right), for **canyon B**. A vortex that occupies around half the canyon drives the pollutant toward the South wall.

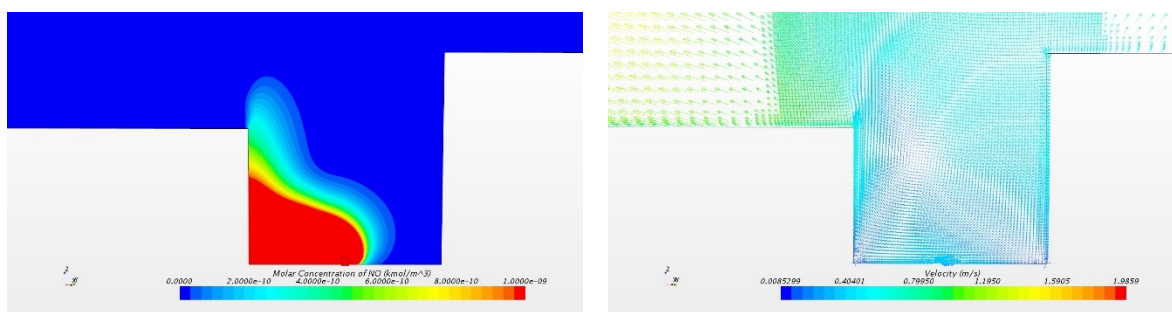


Figure 18. Canyon B: 2D contours of NO molar concentration (kmol m^{-3} ; $1 \text{ kmol/m}^3 = 30 \cdot 10^9 \mu\text{g/m}^3$) obtained for canyon A on a vertical plane intersecting the source (left) and velocity vectors in the same plane for case 2: 17/08/2018, 11:00 UTC.

3.3.2.3 Case 17/08/2018, 14:00 UTC

This case refers to a day condition, with both the canyon A walls painted, but only the North one is activated from the sun UV radiation because the other is in the shadows. The boundary conditions for this case are provided in Table 2 and Table 3 (third line). The wind comes from the North direction (i.e. the direction of the wind forms and angle of 8° with the North-South direction). The domain mesh surrounding the buildings has been rotated in order to have the inlet surface perpendicular to the wind direction, as shown in Figure 19.

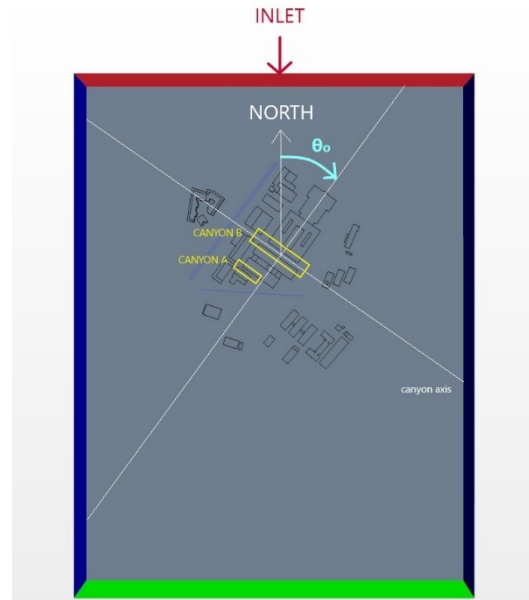


Figure 19. Orientation of the domain for case 3: 17/08/2018, 14:00 UTC.

In this case, the direction of the wind forms an angle of 45° with respect to the axes of the canyons. Figure 20 shows the streamlines colored as a function of the wind velocity obtained for this case. The wind in this case comes from the opposite direction with respect to the first case (night), and therefore the vortices within the canyon in this case show a rotation in the opposite direction with respect to the night case. Two similar vortices are formed within the canyons A and B, that do not cover the entire length of the canyons because are broken by a mixing flow in the middle of the canyon due to the inclination of the canyon with respect to the wind direction. Figure 21 shows that the plumes are close to the North wall, but for canyon A the plume occupies almost the whole volume between the walls.

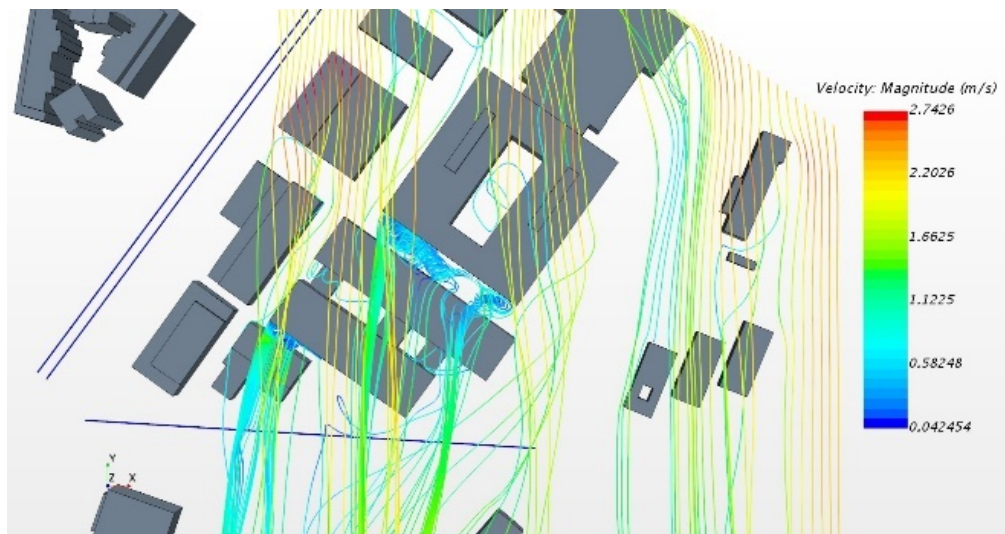


Figure 20. Streamlines obtained for case 3: 17/08/2018, 14:00 UTC.

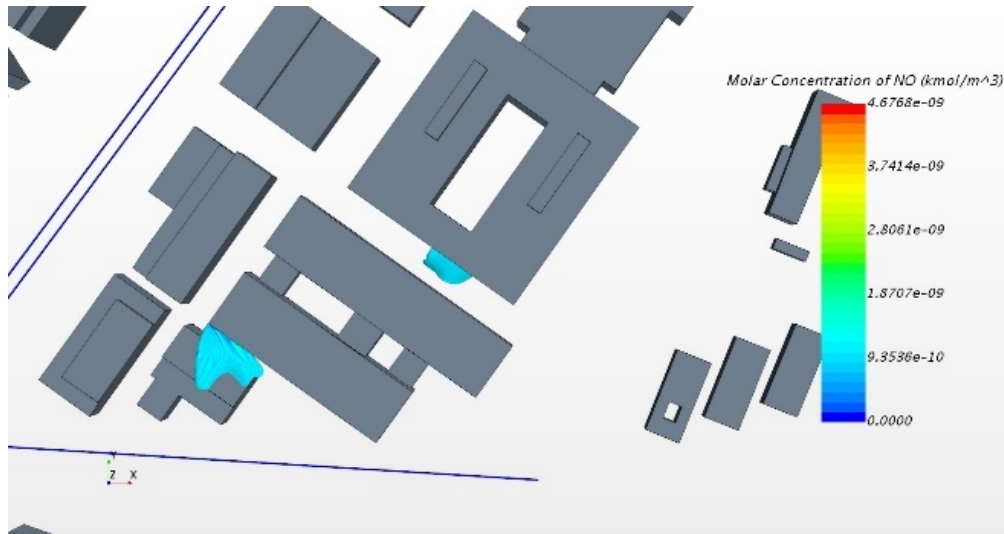


Figure 21. 3D contours of NO molar concentration (kmol m^{-3} ; $1 \text{ kmol/m}^3 = 30 \cdot 10^9 \mu\text{g/m}^3$) obtained for case 3: 17/08/2018, 14:00 UTC 14.

This result is underlined by Figure 22. The pollutant removal from canyon A in this case occurs at the top of the North wall.

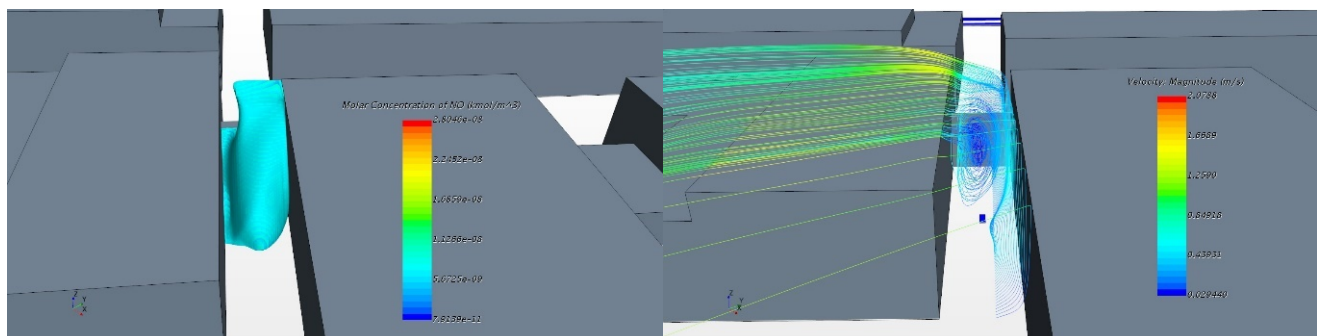


Figure 22. Canyon A. Streamlines (left) and 3D contours of NO molar concentration (kmol m^{-3} ; $1 \text{ kmol/m}^3 = 30 \cdot 10^9 \mu\text{g/m}^3$) (right) obtained for case 2: 17/08/2018, 14:00 UTC.

Figure 23 shows the comparison of NO pollutant concentration on a vertical surface near the source in the two cases.

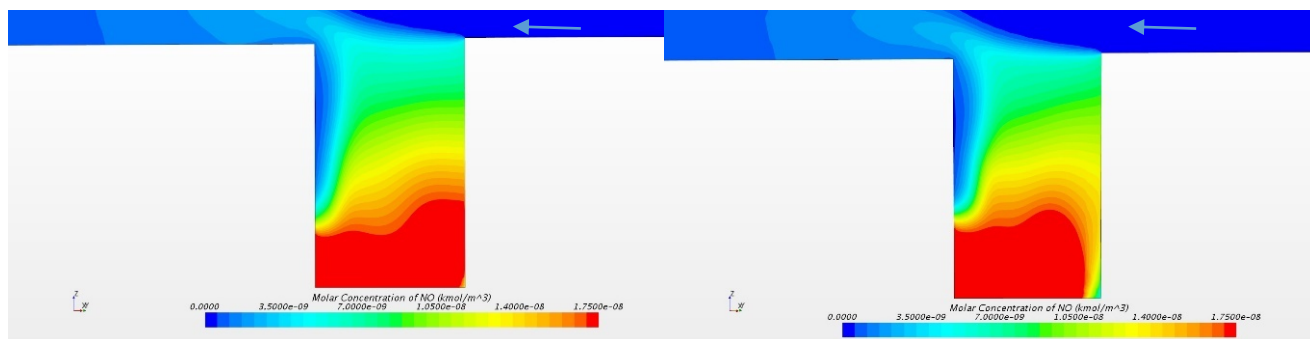


Figure 23. Canyon A: contours of NO molar concentration (kmol m^{-3} ; $1 \text{ kmol/m}^3 = 30 \cdot 10^9 \mu\text{g/m}^3$) obtained for case 3: 17/08/2018, 14:00 UTC. Left: PC absorption is not activated; right: PC absorption is activated.

The Figure provides a comparison between the case with no photocatalytic effect (left) and the case where the photocatalytic effect has been activated (right). A reduction of NO concentration is observed in the region close to the painted surface (North wall). Figure 24 shows the pollutant concentration obtained on the North and South walls of canyon A in the case of non-activated vs. activated photocatalytic effect.

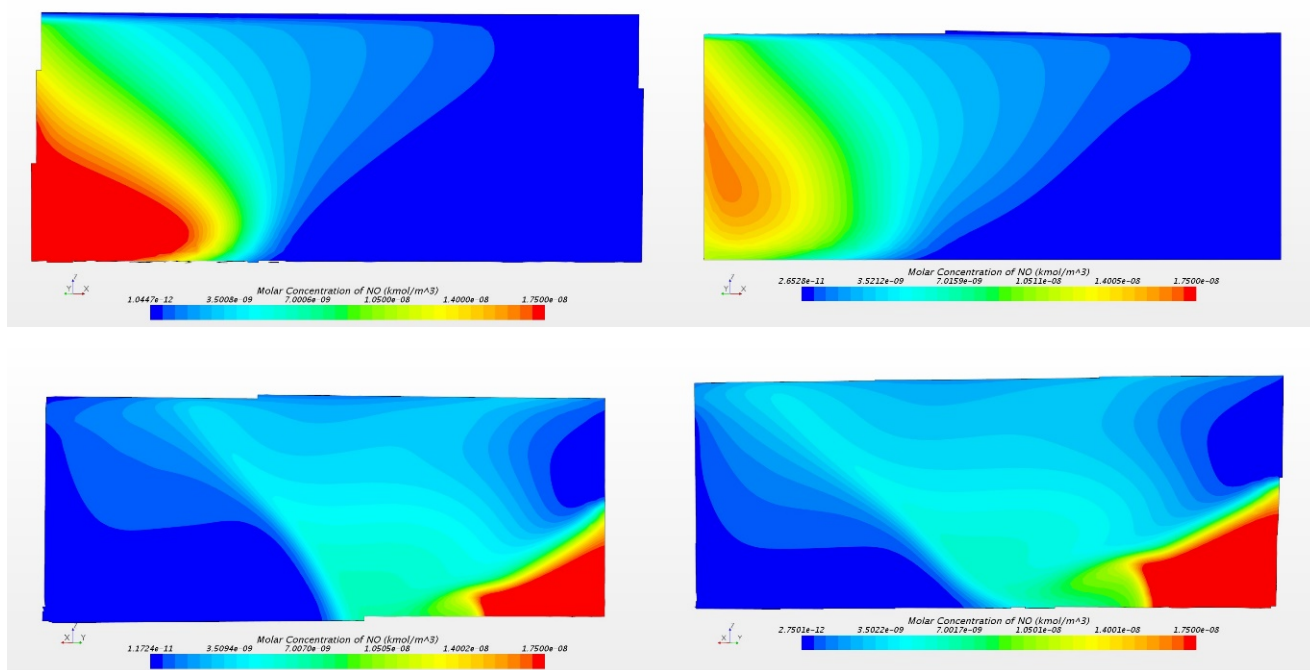


Figure 24. Canyon A: contours of NO molar concentration (kmol m^{-3} ; $1 \text{ kmol/m}^3 = 30 \cdot 10^9 \mu\text{g/m}^3$) obtained for case 2: 17/08/2018, 14:00 at the North wall (top) and at South wall (bottom). Left: PC absorption is not activated; right: PC absorption is activated

As expected, the photocatalytic effect is observed near the North wall, as this is the only wall where the photocatalytic effect has been activated. Figure 25 shows a plot of the NO concentrations near the source along the z vertical direction, at 25cm and 50cm distance from the North wall. The Figure shows that in the lower part of the canyon, a reduction of pollutant concentration up to 40% can be obtained near the wall.

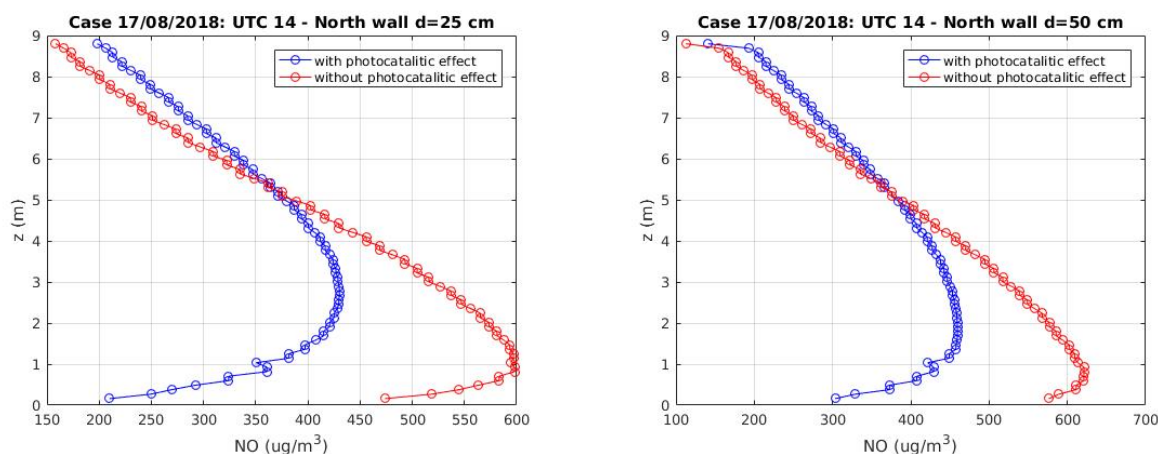


Figure 25. Canyon A: profiles of NO mass concentration ($\mu\text{g m}^{-3}$) obtained for case 3: 17/08/2018, 14:00 UTC. Left: profiles of NO mass concentration ($\mu\text{g m}^{-3}$) at a distance of 25 cm from the North wall; right: NO concentration profile at 50cm distance from the North wall.

Finally, Figure 26 shows the pollutant concentration on a vertical plane near the source (left) and the velocity vectors on the same plane (right), for **canyon B**. A vortex that occupies the canyon drives the pollutant toward the North wall.

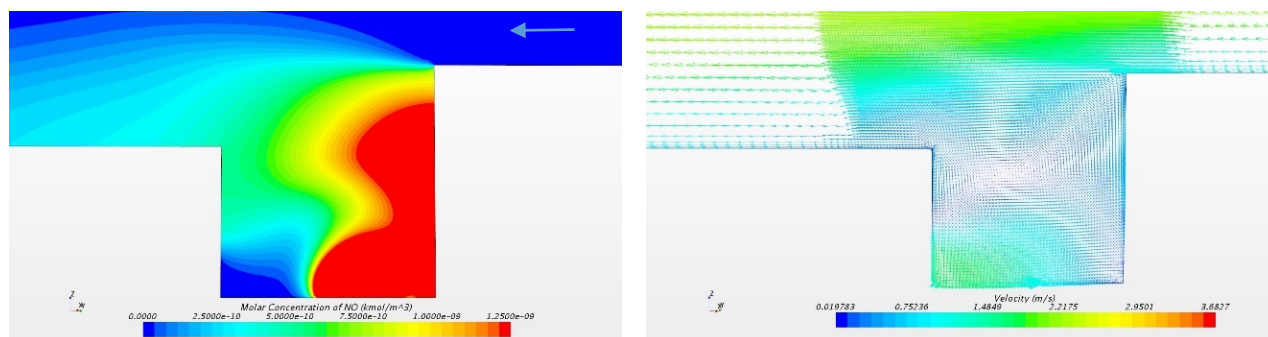


Figure 26. Canyon B: 2D contours of NO molar concentration (kmol m^{-3} ; $1 \text{ kmol/m}^3 = 30 \cdot 10^9 \mu\text{g/m}^3$) obtained for canyon A on a vertical plane intersecting the source (left) and velocity vectors in in the same plane (right) for case 3: 17/08/2018, 14:00 UTC.

3.4 Winter and transition seasons

The action of photocatalytic coatings during other seasons depends both on the different meteorological conditions (wind direction and velocity, air temperature) and on the different solar radiation. To focus on just the dependence of the effectiveness on the change in temperature and incident solar radiation, it was chosen to keep the wind direction and wind speed fixed, or better to analyse two cases with wind direction and wind velocity module similar to those measured for the case 17/08/2018 at 14 UTC. The dependence of the effectiveness of the photocatalytic coating and other PCSs on wind direction is instead more properly the objective of D6.2. In particular, two cases have been chosen: for winter, the day 04/01/2018 at UTC 12 and for transition (spring-autumn) conditions, the day 17/04/2018 at UTC 12. The meteorological conditions relative to these days are provided in Table 6. Hourly measured data for wind direction, air velocity and temperature and sun radiation at the Silvani meteorological station were provided by ARPAE Environmental Protection Agency through the Dext3r database (<http://www.smr.arpa.emr.it/dext3r/>), while the temperatures on the building facades and on the street have been evaluated by a lumped model according with Athamena et al. (2018)

Day	UTC time	Wind direction (°) and wind velocity (m/s)	Tair (°C)	Twalls (°C)	Tstreet (°C)
04/01/2018	12:00	14° – 1.1	10.5	12	8
17/04/2018	12:00	12° – 2.3	22.2	24	18

Table 6. Wind and temperature (air, walls and street) data used for setting the boundary conditions in the winter and spring cases.

From the total solar radiation contribution, by assuming that the photocatalytic action is proportional to the energy carried by the UV fraction of the total sun radiation to the surfaces, the pollutant flux at the surfaces has been modified according with Staub de Melo and Triches (2012). The results in the two cases are provided in the following subsections.

3.4.1 Winter case: 04/01/2018, 12:00 UTC

This case refers to a day condition, with all the walls activated by the sun UV radiation. The boundary conditions for this case are provided in Table 6 (first line). The wind comes almost from the North direction (i.e. the direction of the wind forms an angle of 14° with the North-South direction). The domain mesh surrounding the buildings has been rotated in order to have the inlet surface perpendicular to the wind direction. In this case, the direction of the wind is almost the same as that obtained for the third summer case in the previous section. Figure 27 shows the streamlines colored as a function of the wind velocity obtained for this case. Within the two canyons, two vortices similar to those obtained for the third summer case are formed, with the differences outlined in the following.

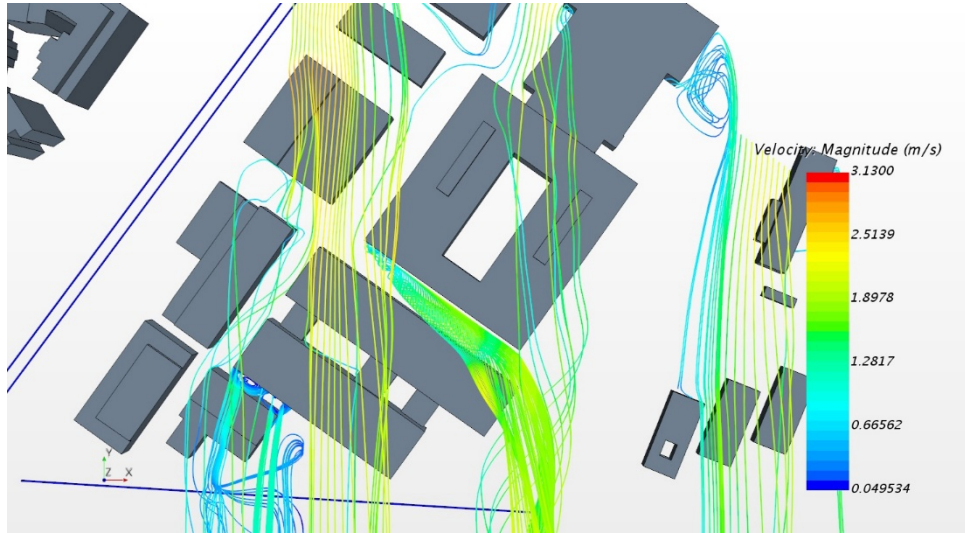


Figure 27. Canyon A. Streamlines obtained for case 04/01/2018, 12:00 UTC.

In canyon B, the vortex dimension increases along the canyon, while in the summer case it is interrupted near the position of the pollutant source. While the vortex occupies the whole canyon A in the winter case, it occupied only the half from the source to the canyon North-West opening during summer. These differences reflect in different shapes of the plumes, as shown by Figure 28.

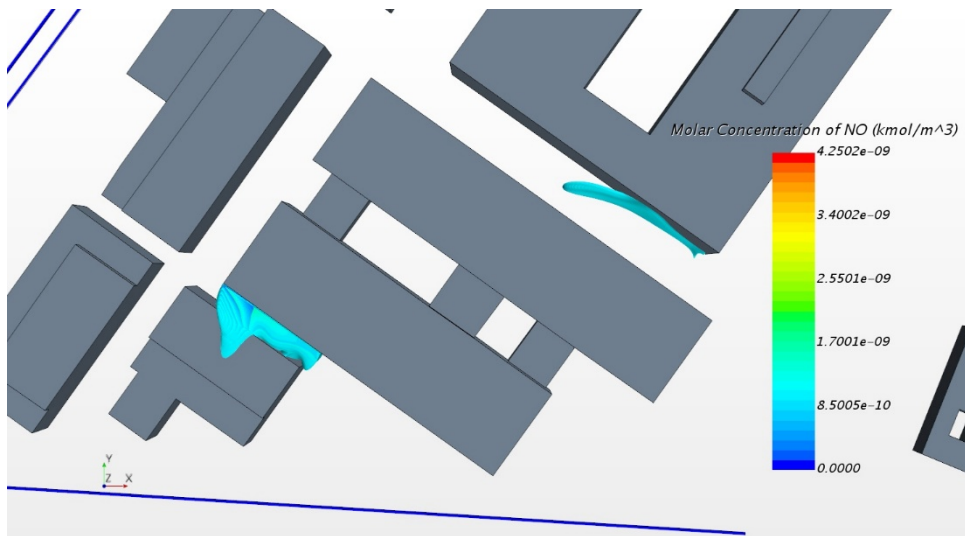


Figure 28. Canyon A. 3D contours of NO molar concentration (kmol m^{-3} ; $1 \text{ kmol/m}^3 = 30 \cdot 10^9 \mu\text{g/m}^3$) obtained for case 04/01/2018, 12:00 UTC.

Figure 28 shows that for winter case the NO concentration plume in canyon B is thin and flat near the North wall, while in canyon A the NO plume is larger than that obtained for summer in similar wind conditions. Figure 29 shows the NO concentration contours obtained near the source in the two canyons.

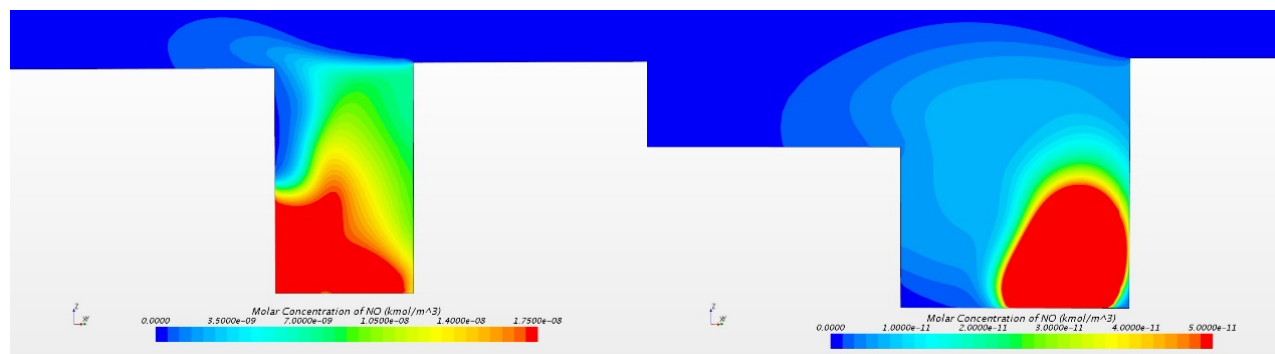


Figure 29. 2D contours of NO molar concentration (kmol m^{-3} ; $1 \text{ kmol/m}^3 = 30 \cdot 10^9 \mu\text{g/m}^3$) obtained for canyon A (left) and B (right) on a vertical plane near the source for case 04/01/2018, 12:00 UTC.

3.4.2 Transition season case: 17/04/2018, 12:00 UTC

This case refers to a day condition in spring, with all the walls activated from the sun UV radiation. The boundary conditions for this case are provided in Table 6 (second line). The wind comes almost from the North direction (i.e. the direction of the wind forms and angle of 12° with the North-South direction). The domain mesh surrounding the buildings has been rotated in order to have the inlet surface perpendicular to the wind direction. In this case, the direction of the wind is almost the same as that observed during the third summer case discussed in the previous section. Figure 30 shows the streamlines colored as a function of the wind velocity obtained for this case. Within the two canyons, two similar vortices as those obtained for the third summer case are formed, with some differences which will be discussed in the following.

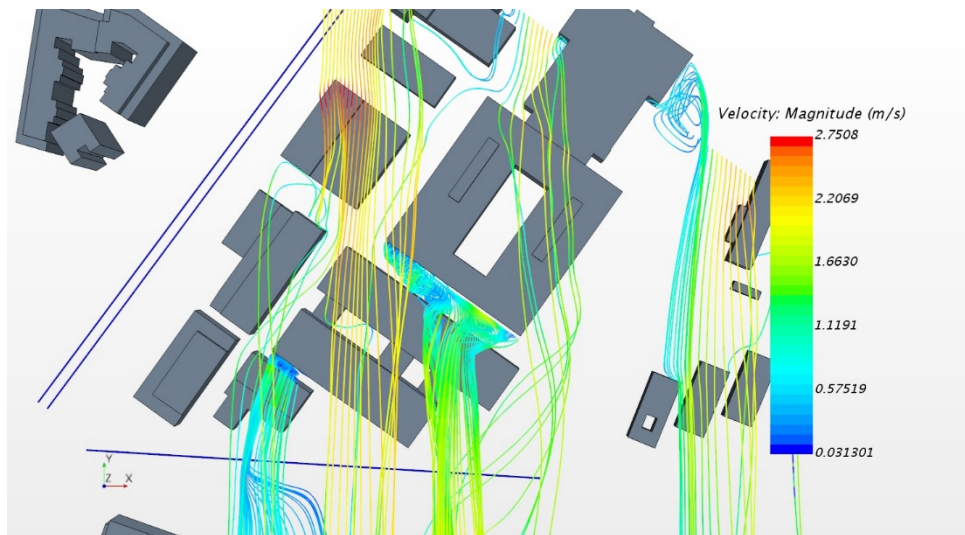


Figure 30. Canyon A. Streamlines obtained for case 17/04/2018, 12:00 UTC.

In canyon B, the vortex dimension is constant along the canyon, while in the summer case it was interrupted near the position of the pollutant source. By comparing this vortex with the winter case, one can observe that in this case, more mixing at the top of the canyon occurs. In canyon A, more mixing is

observed at the top with respect to the summer and winter cases. These differences reflect in different shapes of the plumes, as shown by Figure 31.

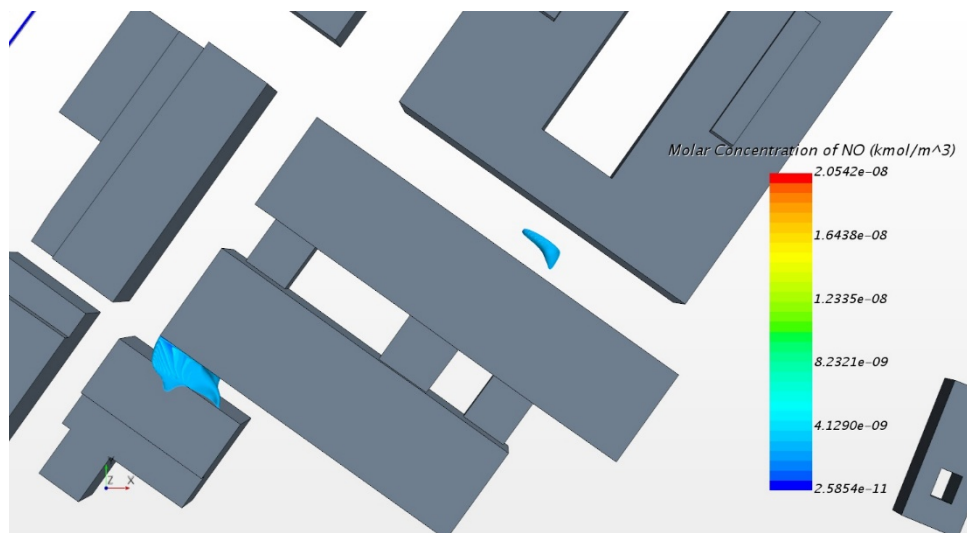


Figure 31. Canyon A. 3D contours of NO molar concentration (kmol m^{-3} ; $1 \text{ kmol/m}^3 = 30 \cdot 10^9 \mu\text{g/m}^3$) obtained for case 17/04/2018, 12:00 UTC.

Figure 31 shows that for spring case the NO concentration plume in canyon B is thin and flat near the source, while in canyon A, the NO plume is smaller than those obtained for winter and summer cases with similar wind speeds and directions. Figure 32 shows the NO concentration contours obtained near the source in the two canyons.

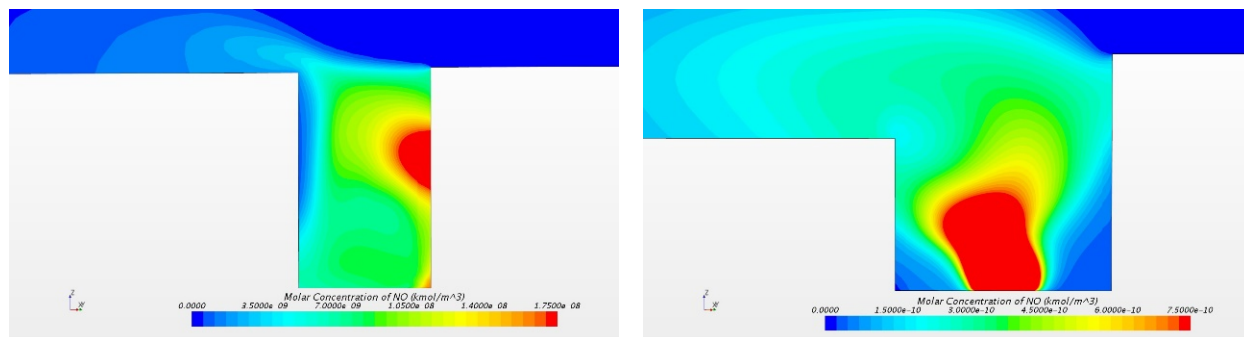


Figure 32. 2D contours of NO molar concentration (kmol m^{-3} ; $1 \text{ kmol/m}^3 = 30 \cdot 10^9 \mu\text{g/m}^3$) obtained for canyon A (left) and B (right) on a vertical plane near the source for case 17/04/2018, 12:00 UTC.

3.4.3 Comparison between the three cases

Figure 33 shows the comparison between the NO profiles obtained near the North wall of canyon A for the three cases: summer (17/08/2018, 14:00 UTC), winter (04/01/2018, 12:00 UTC) and spring (17/04/2018, 12:00 UTC). As discussed previously, to focus on just the dependence of the effectiveness of the photocatalytic coatings on the changes in solar radiation and temperature values, cases with similar wind direction and wind velocity module were chosen. The NO concentrations obtained for winter and spring cases are lower than those obtained for summer case up to 4 m, while going to higher heights

the spring case presents the highest concentration. However, these plots show that the effect of photocatalytic coatings locally can strongly depend on the seasonal boundary conditions.

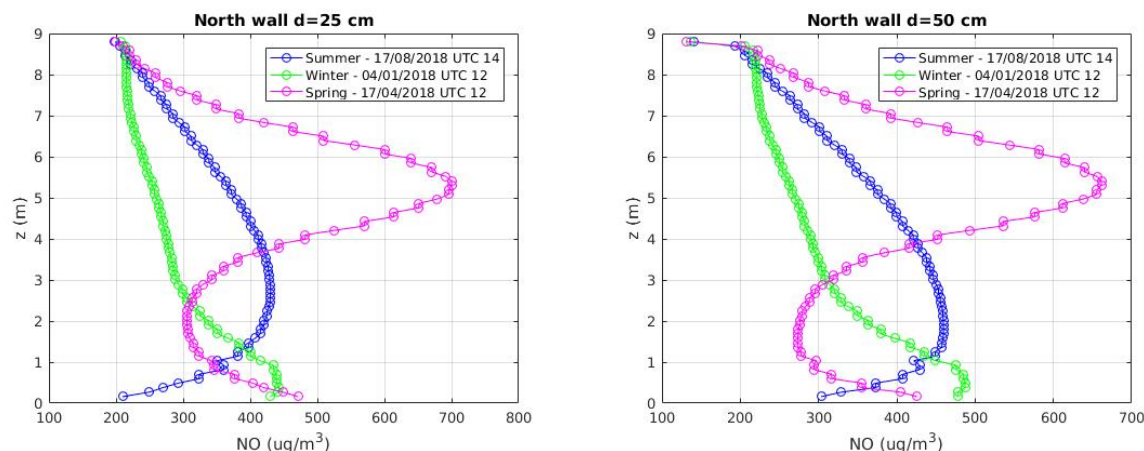


Figure 33. Canyon A: profiles of NO mass concentration ($\mu\text{g m}^{-3}$) obtained for cases: summer (17/08/2018, 14:00 UTC), winter (04/01/2018) and spring (17/04/2018). Left: profiles of NO mass concentration ($\mu\text{g m}^{-3}$) at 25cm distance from the North wall: right: NO concentration profile at 50cm distance from the North wall.

4. Conclusions

During summer 2018 an experimental campaign was deployed in two street canyons at the Lazzaretto site in the city of Bologna to analyse the effectiveness of photocatalytic coatings. The instrumental setup and the results of the experimental campaign are presented in D3.8. In particular, photocatalytic coatings have been applied in the walls of one of the two street canyon and over the road between the walls of the canyon. In addition, some controlled pollutant releases with a known pollution source (one EURO-2 diesel car) were setup in each of the two street canyons. Two mobile laboratories, equipped for continuous measurements of air pollutants such as nitrogen oxides (NO_x , NO, and NO_2), carbon monoxide (CO), ozone (O_3), sulfur dioxide (SO_2) with a 1-min time resolution were placed along the two street canyons. Additional instrumentation for the measurement of meteorological and turbulence variables was also deployed on the roof of the ARPAE vans and over the roofs of the two canyons to measure wind speed, wind direction, temperature and humidity both inside as well as above the canyons.

Through a CFD-based approach, the local distribution of NO concentration within the canyon has been obtained for the same conditions of the experiments. From the comparison of the results obtained from CFD simulations with one of the experiments conducted during the summer and described in D3.8, a calibration of the model of pollutant reduction at the wall has been set. Then, the model has been applied to other summer conditions encountered during the experimental campaign and verified by comparing the results with the experimentally observed values. The numerical results have shown a good agreement with the experimental results. Moreover, simulations have shown that the NO reduction is a very local function of space, and can reach higher values than those observed within the experiments (D3.8) (10-20%), even up to 40-50% near the painted walls. The results also showed that the NO reduction is a function of the atmospheric conditions (wind velocity and direction, temperature, solar radiation) coupled to the geometry of the buildings. In a street canyon, when the walls and the street are exposed to the maximum UV sun light (i.e. around noon), a strong reduction of pollutant

concentration in the lower part of the street canyon is observed. In winter, during sunny days, the reduction at noon can be higher than that observed in a summer afternoon, when some of the walls are in the shadows. In order to generalize these results, a deeper comprehension and testing of the models for the photocatalytic surface reactions are still needed. However, it is important to remark here that all the relevant variables were measured during the tests performed within the experimental campaigns in order to verify the theoretical and modeling approach adopted in the CFD simulations performed in this work.

5. References / Bibliography

Athamena, K., Sini, J.F., Rosant, J.M., & Guilhot, J., 2018. Numerical coupling model to compute the microclimate parameters inside a street canyon. Part I: Methodology and experimental validation of surface temperature. *Solar Energy*, 174, 1237-1251.

Ballari, M.M., & Brouwers, H.J.H., 2013. Full scale demonstration of air-purifying pavement. *Journal of Hazardous Materials*, 254-255, 406-414.

Boonen, E., & Beeldens, A., 2014. Recent photocatalytic applications for air purification in Belgium. *Coatings* 4 (3), 553-573.

EEA (European Environment Agency), 2016. EMEP/EEA air pollutant emission inventory guidebook 2016. Technical guidance to prepare national emission inventories. European Environment Agency, Copenhagen, available at <https://www.eea.europa.eu/publications/emep-eea-guidebook-2016>, last accessed 4 Feb 2019.

Folli, A., Pochard, I., Nonat, A., Jakobsen, U.H., Shepherd, A. M., & Macphee, D.E., 2010. Engineering Photocatalytic Cements: Understanding TiO₂ Surface Chemistry to Control and Modulate Photocatalytic Performances. *Journal of the American Ceramic Society*, 93, [10], 3360-3369.

Gallus, M., Akylas, V., Barmpas, F., Beeldens, A., Boonen, E., Boréave, A., Cazaunau, M., Chen, H., Daële, V., Doussin, J.F., Dupart, J.F., Gaimoz, C., George, C., Grosselin, B., Hermann, H., Ifang, S., Kurtenbach, R., Maille, M., Mellouki, A., Miet, K., Mothes, F., Moussiopoulos, N., Poulain, L., Rabe, R., Zapf, P., & Kleffmann, J. 2015. Photocatalytic de-pollution in the Leopold II tunnel in Brussels: NO_x abatement results. *Building and Environment*, 84, 125-133.

Guerrini, G.L., 2012. Photocatalytic performances in a city tunnel in Rome: NO_x monitoring results. *Construction and Building Materials*, 27, 165-175.

Janus, M. & Zajac, K., 2016. Concretes with Photocatalytic Activity. In: *High Performance Concrete Technology and Applications*, Salih Yilmaz and Hayri Baytan Ozmen (Eds.), ISBN: 978-953-51-2651-5, Open Access peer-reviewed Edited Volume, inTechOpen.

Jeanjean, A.P.R., Gallagher, J., Monks, P.S., & Leigh, R.J., 2017. Ranking current prospective NO₂ pollution mitigation strategies: An environmental and economic modelling investigation in Oxford Street, London. *Environmental Pollution* 225, 587-597.

Lasek, J., Yu, Y.H., & Wu, J.C., 2013. Removal of NO_x by photocatalytic processes. *Journal of Photochemistry and Photobiology C: Photochemistry Reviews*, 14, 29-52.

Liang, S., Zheng, T., Liu, R., Fang, H., Tsay, S. C., Running, S., 2006. Estimation of incident photosynthetically active radiation from MODIS data. *Journal of Geophysical Research*, 111, D15208.

Mills, 2007. A. *Removal of nitric oxide: Modified ISO 22197-1:2007. "Fine ceramics – Test method of air-purification performance of semiconducting photocatalytic materials."* Queen's University Belfast.

Maggos, Th., Plassais, A., Bartzis J.G., Vasilakos, Ch., Moussiopoulos, N., & Bonafous, L., 2008. *Photocatalytic degradation of NO_x in a pilot street canyon configuration using TiO₂-mortar panels. Environmental Monitoring and Assessment, 136, 35-44.*

Palacios, M., Nùñez, L., Pujadas, M., Fernández-Pampillón, J., Germán, M., Sánchez, B.S., & Cabrero, B.S., 2015. *Estimation of NO_x deposition velocities for selected commercial photocatalytic products. WIT Transactions of the Built Environment, 168, 729-740.*